OKINAWA INSTITUTE OF SCIENCE AND TECHNOLOGY
GRADUATE UNIVERSITY

Thesis submitted for the degree

Doctor of Philosophy

Ultrafast spatiotemporal control of photocarriers in doped semiconductors

by

E Laine Wong

Supervisor: **Keshav M. Dani**

July, 2018

Declaration of Original and Sole Authorship

I, E Laine Wong, declare that this thesis entitled *Ultrafast spatiotemporal control of photocarriers in doped semiconductors* and the data presented in it are original and my own work.

I confirm that:

- No part of this work has previously been submitted for a degree at this or any other university.

- References to the work of others have been clearly acknowledged. Quotations from the work of others have been clearly indicated, and attributed to them.

- In cases where others have contributed to part of this work, such contribution has been clearly acknowledged and distinguished from my own work.

- None of this work has been previously published elsewhere, with the exception of the following:

    Publication:

    E Laine Wong, Andrew J. Winchester, Vivek Pareek, Julien Madéo, Michael K. L. Man and Keshav M. Dani. Pulling apart photoexcited electrons by photo-inducing an in-plane surface electric field. Science Advances (Accepted).

    Patent:

E Laine Wong, Michael K. L. Man and Keshav M. Dani. Ultrafast control of photoexcited particles with high spatial resolution. US Provisional Patent Application Number: **US 62/660,818**.

Date: July, 2018

Signature:

Abstract

Ultrafast spatiotemporal control of photocarriers in doped semiconductors

Control of the spatial and temporal dynamics of photoexcited charge carriers at the surfaces and interfaces of semiconducting materials is pertinent to many of modern technologies such as solar cells, photodetectors and other optoelectronic devices. In inhomogeneous materials such as nanostructured materials, spatial variations in carrier dynamics are inherent via the material design and accordingly allow for improvements in device performance e.g. transport of electrons from donor to acceptor regions in photovoltaic devices. On the other hand, one can also create spatial inhomogeneity in the carrier dynamics in homogeneous systems by using a non-uniform photoexcitation profile. This would have the advantage that the control of the carrier dynamics could be more flexible and not tied down to the fixed material design. In principle, photoexcitation even with a simple Gaussian beam could result in nontrivial inhomogeneous carrier dynamics within the full-width-half-maximum (FWHM) of the optical spot. However, in typical ultrafast spectroscopy measurements performed thus far, one averages out the photocarrier response over the excitation spot and spatial variations therein are inaccessible.

In this thesis, we create nontrivial spatiotemporal dynamics of the photoexcited electrons in a homogeneous Zn-doped GaAs using the spatial intensity variation in a simple Gaussian photoexcitation beam. We image these dynamics using time-resolved photoemission electron microscopy (TR-PEEM) - a technique offering both high temporal and

spatial resolutions. In particular, we demonstrate the spatial redistribution of the photoexcited electrons in two different regimes: (I) the early time delays where we control the vertical transport of electrons to the sample surface and (II) at long time delays where we manipulate the lateral distribution of the electrons along the sample surface.

In the first study, we achieve spatial variations in the screening process of the intrinsic surface field, which influences the vertical drift of photoexcited electrons from the bulk to the sample surface. Combined with the occurrence of Auger recombination in regions of higher intensity, we see a depletion in the electron population at the center, with a gain just away from the center. We show control of these processes and how they affect the electron distribution on the sample surface in nontrivial ways.

In the second study, we show that at long time delays the spatially varying screening process leads to the creation of lateral fields along the sample surface. These highly local and spatially varying lateral fields then act upon the photoexcited electrons, eventually pulling them apart into two distinct distributions. Using a simple model that explains the experimental data, we also show the possibility of generating near-arbitrary lateral fields and thus controlling electrons on the sample surface in more general ways.

In conclusion, this thesis demonstrates the capability to create and control nontrivial spatiotemporal dynamics of the photoexcited electrons even in a homogeneous semiconductor by exploiting the intensity variation of an ultrafast light pulse. This capability could lead to a promising new handle for use in high-speed optoelectronic devices.

Acknowledgement

First of all, I would like to express my sincerest gratitude to Professor Keshav Dani for his continuous support, guidance and patience throughout the many years of my PhD research in OIST. I have learnt a great deal from him, both in terms of research as well as the necessary soft skills for a successful career later in life. Next, I would like to express my sincere thanks to Professor Bala Murali Krishna Mariserla and Dr. Michael Man Ka Lun for their immense help and support on the HHG setup and the PEEM instrument, and for their invaluable advice and discussions on the topics. My sincere thanks also go to Dr. Julien Madéo, Andrew Winchester and Vivek Pareek for their help and the many insightful discussions on my research projects. A special thanks to Yumi-san for all her help throughout the years with the administrative dealings. I would also like to express my heartfelt gratitude to the past and present staffs at the Student Support Section for making me feel welcome and at home since my very first day in Okinawa and for their continual support throughout my stay in OIST and in Okinawa.

To my parents

Wong Yoon Sim & Tan Kim Choo

Contents

List of Figures

List of Tables

Outline

This thesis is organized as follows:

Chapter 1 describes the rising need for a single probing method that combines high spatial and temporal resolutions for the study of carrier dynamics in semiconductors. It then briefly examines the spatial and temporal scale required to access the photocarrier dynamics within the photoexcitation spot. The chapter then goes on to discuss the strengths and weaknesses of three newly developed techniques that have been showing great potential for the study of charge carrier dynamics in semiconductors with both high spatial and temporal resolutions.

Chapter 2 describes in further detail time-resolved photoemission electron microscopy (TR-PEEM) that is used for the studies described in this thesis. The chapter first looks at the operating principle and the light sources available for a photoemission electron microscope. It then goes on to provide a brief overview of the previous studies conducted using TR-PEEM.

Chapter 3 describes in detail the setup of the ultrafast pump-probe spectroscopy used and the introduction of the ultrafast pulses into the electron microscope. The second part of this chapter covers the preparation and characterization of the Zn-doped GaAs sample. This is then followed by a discussion of the optical and electronic properties of the sample that are crucial to the understanding of the experimental results presented in Chapter 4

and Chapter 5.

Chapter 4 first demonstrates the inhomogeneous photocarrier dynamics within the FWHM of the photoexcitation spot. The chapter then discusses the spatial variation in the partial screening of the intrinsic surface field and the Auger recombination that results in the depletion of electrons near the center of the spot and the vertical drift of electrons to the surface further away from the center. It is then demonstrated that the ratio between the two spatial regions of influx and depletion of electrons can be controlled via tuning the photoexcitation intensity. Lastly, the impact of the inhomogeneous photo-carrier dynamics on the spatiotemporal distribution of the electrons at the sample surface is discussed.

Chapter 5 first presents the experimental data showing the eventual separation of the photoexcited electrons within the optical spot into two resolvable distributions. The chapter then demonstrates the control of the degree and rate of separation of the charge carriers via the spatial profile and the intensity of the photoexcitation beam. The chapter then goes on to provide both an intuitive and a quantitative model to explain the underlying charge transport phenomena and to reproduce the salient features of the experimental data.

Chapter 1

Imaging the distribution and flow of photocarriers

1.1 Chapter overview

This chapter briefly discusses the motivation to study the photoexcited charge carrier dynamics at the surfaces of semiconductors with simultaneous high spatial and temporal resolutions. The chapter then briefly examines the pros and cons of three emerging techniques with the desired high spatial and temporal resolutions followed by a brief overview of the studies that have been successfully carried out with these techniques.

1.2 Study of spatiotemporal dynamics of photocarriers

1.2.1 Why study spatiotemporal dynamics?

The spatial and temporal dynamics of photoexcited charge carriers at the surfaces and interfaces of semiconductors is of vital importance to the proper design and performance of many modern technologies such as solar cells, photocatalytic processes and other opto-electronic devices. For example, the length scale of the transport of hot carriers in hybrid perovskite thin film might be key to improving the efficiency of solar cells [1]. In the

case of photocatalytic processes, the efficient separation of the photoexcited electron-hole pairs and the transport of the charge carriers to the material surfaces are amongst the few rate determining steps of the redox reactions [2]. As such, manipulation of the spatiotemporal distribution of the charge carriers at the material surfaces could potentially allow for temporally-controlled photocatalytic activities to happen at selected spatial locations. Even for homogeneous semiconducting materials, spatial variation in the photocarrier dynamics can be induced by harnessing the rich variety of intensity-dependent physical processes that can occur in semiconductors. The capability to manipulate the spatial and temporal distribution of the photocarriers within the optical spot by utilizing the non-uniform photoexcitation intensity profile could potentially lead to the control of photocarriers beyond the diffraction limit of light. The continual development of these scientific and technological aims necessitates the development of techniques that are capable of imaging the photocarrier dynamics with simultaneous high spatial and temporal resolutions.

1.2.2 How to study spatiotemporal dynamics? (Overview)

The natural timescale of electron dynamics such as thermalization, scattering and recombination largely falls between the nanosecond to femtosecond range i.e. $10^{-9} - 10^{-15}$ seconds. To measure such a short burst of event, one would require an even faster probe. To date, ultrafast pump-probe spectroscopy remains one of the widely used technique to access such transient dynamics. With this technique, an ultrafast pump pulse is used to first excite the sample and a time-delayed probe pulse is used to monitor the pump-induced change in the optical properties of the sample. The temporal dynamics of the photoexcited charge carriers can then be inferred from the change in the measured transmission or reflection of the probe pulse as a function of the time delay between the arrivals of the pump and the probe pulses. The temporal resolution of this technique is typically only limited by the laser pulse duration which is in the range of 10s – 100s of femtoseconds. Despite the success of pump-probe spectroscopy in unveiling many important physical phenomena

in semiconductors, its nature of bulk averaging the measured quantities renders it inapt for the study of spatially inhomogeneous dynamics nor photocarrier transport.

Microscopy techniques, on the other hand, are often used to image spatially varying structures and motions in molecular and biological samples. The spatial resolution required for the study of photocarrier dynamics in semiconductors is typically in the micron to nanometer scale. The vast selection of commercially available optical and electron microscopes with the desired spatial resolution has aided in the fruition of several new techniques that interfaces the pump-probe spectroscopy with the microscopy techniques to allow for the study of photocarrier dynamics with simultaneous high spatial and temporal resolutions. In the following section, the strengths and weaknesses of three such techniques i.e. ultrafast pump-probe microscopy, scanning ultrafast electron microscopy and time-resolved photoemission electron microscopy will be further discussed in details.

1.3   Techniques to study spatiotemporal dynamics of photocarriers

1.3.1   Ultrafast pump-probe microscopy

Ultrafast pump-probe microscopy is an all-optical technique that extends the functionality of a conventional ultrafast pump-probe spectroscopy with the use of an optical microscope. Compared to the other two techniques, this technique is comparatively easy to setup and does not require any ultrahigh vacuum system. This technique retains the femtosecond temporal resolution of the pump-probe spectroscopy while also offering high spatial resolution of a few hundreds of nanometers. To track the motion of the charge carriers, the probe beam is scanned across the region-of-interest relative to the position of the pump beam. Similar to pump-probe spectroscopy, the charge carrier dynamics is indirectly inferred from the measurement of the photo-induced change in the optical properties of the sample. This technique has allowed researchers to reveal the heterogeneous charge carrier

dynamics within single nanorod [3] and perovskite grains [4], as well as to study the drift and diffusion phenomena in semiconductor nanostructures [5, 6, 7] and perovskite thin films [1, 8].

1.3.2   Scanning ultrafast electron microscopy

Scanning ultrafast electron microscopy (SUEM) combines the spatial resolution of a scanning electron microscope (SEM) with the temporal resolution of an ultrafast pump-probe setup. In contrast to the optical-pump-optical-probe of the ultrafast pump-probe microscopy technique, SUEM is an optical-pump-electron-probe technique that utilizes an ultrafast electron packet to probe the photocarrier dynamics. The shorter wavelength of the electron probe naturally provides for a higher spatial resolving power. The temporal resolution is however limited to a few picoseconds due to the duration of the secondary electron emission process [9]. SUEM tracks the local populations of the photoexcited electrons and holes by raster scanning the electron probe across the sample surface and measures the photo-induced enhancement or suppression of the secondary electron yield at each locations. Due to the short escape depth, only the secondary electrons from the top few nanometers of the sample are emitted to vacuum and detected, making SUEM a surface sensitive technique. The interpretation of SUEM measurements can be quite complex due to the many factors that can affect the secondary electron emission. For example, the higher average energy of the photoexcited electrons leads to an increase in the secondary electron emission. On the other hand, the presence of the photocarriers also leads to an increased scattering of the secondary electrons thus suppressing the secondary electron emission. A comprehensive review of the working principle and the contrast mechanism of SUEM can be found in [9]. The high spatiotemporal resolution of SUEM has enabled researchers to study the extent of charge carrier separation in a silicon p-n junction [10], the anomalous diffusion regime and spontaneous electron-hole pair separation in an amorphous silicon sample [11], as well as the anisotropic diffusion of hot holes in black phosphorus [12].

1.3.3 Time-resolved photoemission electron microscopy

Time-resolved photoemission electron microscopy (TR-PEEM) interfaces a photoemission electron microscope with an ultrafast pump-probe setup. In contrast to the two techniques described in the previous sections, TR-PEEM maintains the femtosecond temporal resolution of a pump-probe setup while also exploiting the high spatial resolving power of an electron microscope. In addition, TR-PEEM is also a non-scanning technique thus allowing for fast image acquisition. To study the photocarrier dynamics, TR-PEEM uses an optical pump to photoexcite electrons into the conduction band and a time-delayed optical probe to photoemit the photoexcited electrons from the sample. The photoemitted electrons are then collected by the electron microscope to form a series of images that reflect directly the time-delayed spatial distribution of the photoexcited electrons in the sample. Due to the low electron energy, typically in the range of a few electronvolts, only the electrons from the top few nanometers of the sample will be photoemitted, making TR-PEEM a surface sensitive technique. Further details of the TR-PEEM technique and a brief overview of the previous studies carried out using this technique will be discussed in Chapter 2.

1.4 Chapter conclusion

The first part of this chapter described briefly the motivation for investigating the photocarrier dynamics in semiconductors with simultaneous high spatial and temporal resolutions. It then looked at the timescale and spatial resolution required for the studies and the current techniques used i.e. pump-probe spectroscopy and microscopy, for achieving the desired temporal or spatial resolution. The second part then compared the strengths and weaknesses of three emerging techniques that combine the temporal resolution of the pump-probe spectroscopy with the spatial resolution of the microscopy technique. The next chapter will describe in further details the TR-PEEM technique that is used for the studies in this thesis.

Chapter 2

Time-resolved photoemission electron microscopy

2.1 Chapter overview

This chapter starts with a brief introduction to photoemission electron microscopy (PEEM). It then describes the working principle and the available light sources for PEEM. This is then followed by a brief overview of the previous studies conducted using TR-PEEM.

2.2 Photoemission electron microscopy

2.2.1 Introduction

In 1933, with the use of a simple magnetic lens, Brüche first demonstrated that electrons produced via ultraviolet light irradiation and accelerated to high energy could be used for surface imaging (Figure 2.1) [13]. In the following years, this simple instrument was continually improved upon with the inclusion of additional electron lenses, contrast apertures and ultrahigh vacuum systems [13, 14, 15]. Today's PEEM is typically capable of a lateral spatial resolution of better than 15nm as demonstrated by Elmitec PEEM III [16]. An overview of the milestones of PEEM development can be found in [14, 15].
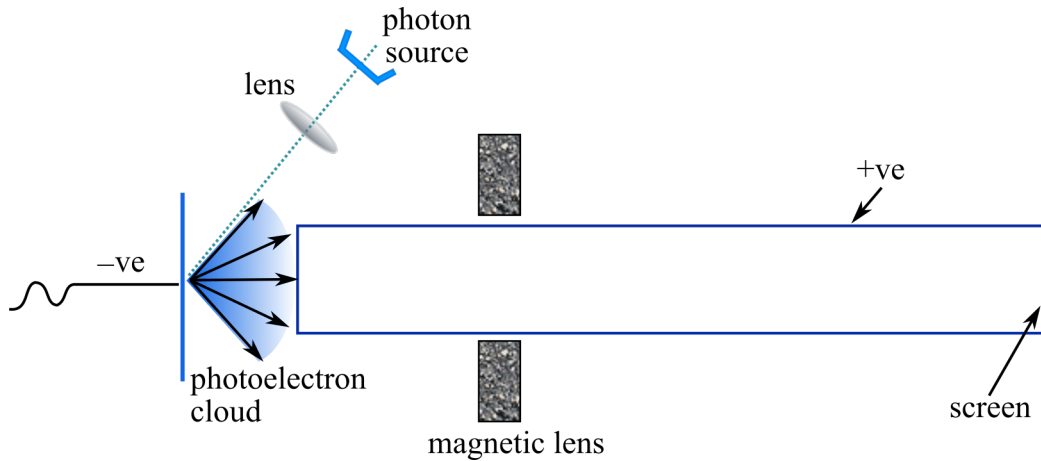
Figure 2.1: Schematic of Brüche's 1st PEEM system [13]

PEEM is a variant of surface electron emission microscopy that is widely used in the studies of surfaces, thin films and nanostructures. Contrary to most electron emission microscopes, PEEM images the sample surface with photoelectrons that are generated by an ultraviolet (UV) or an x-ray light source, as depicted in Figure 2.1. This technique provides information about the electronic structures, chemical and structural composition of the local environment being probed based on Einstein's photoelectric equation of

$$h\nu = \phi + E_B + E_{KE} \tag{2.1}$$

where

$h\nu$ is the energy of incident photon

ϕ is the work function of the sample

E_B is the core level binding energy

E_{KE} is the kinetic energy of the photoelectron

With photon irradiation, there are three potential imaging candidates i.e. photoelectrons, secondary and Auger electrons. Photoelectrons are electrons that are photoemitted directly from the sample by the incident photons. Due to the low photon energy (4.65eV) used for the studies in this thesis, the main imaging candidate is the photoelectrons as any
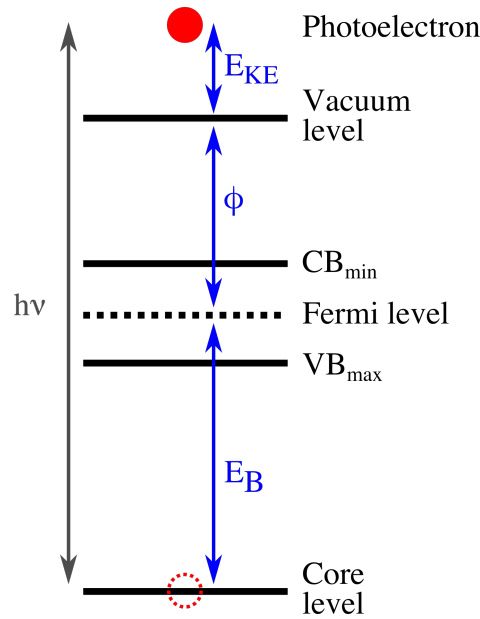
Figure 2.2: Schematic of an energy diagram for the photoelectric equation

additional energy loss from inelastic scatterings will leave the electrons with insufficient energy to overcome the work function of the sample. The following subsection will go on to discuss the theory of operation behind PEEM and the different light sources available for PEEM imaging.

2.2.2   Theory of operation

Our PEEM instrument is a spectroscopic photoemission and low energy electron microscope (SPELEEM) (Figure 2.3) that is also equipped with an electron illumination arm that provides for the capability to perform low energy electron imaging (LEEM) and diffraction (LEED) measurements. As shown in Figure 2.3, both LEEM and PEEM share the same imaging column, differing only in the illumination columns. For PEEM, the illumination column is as simple as shining a UV or an x-ray light onto the sample.

The imaging column, on the other hand, comprises at least three lenses i.e. objective, intermediate and projective lenses, as well as an energy analyzer [17]. The objective lens collects, accelerates and focuses the emitted photoelectrons to the first image plane in the beam separator. The objective lens together with an angle-limiting aperture are the
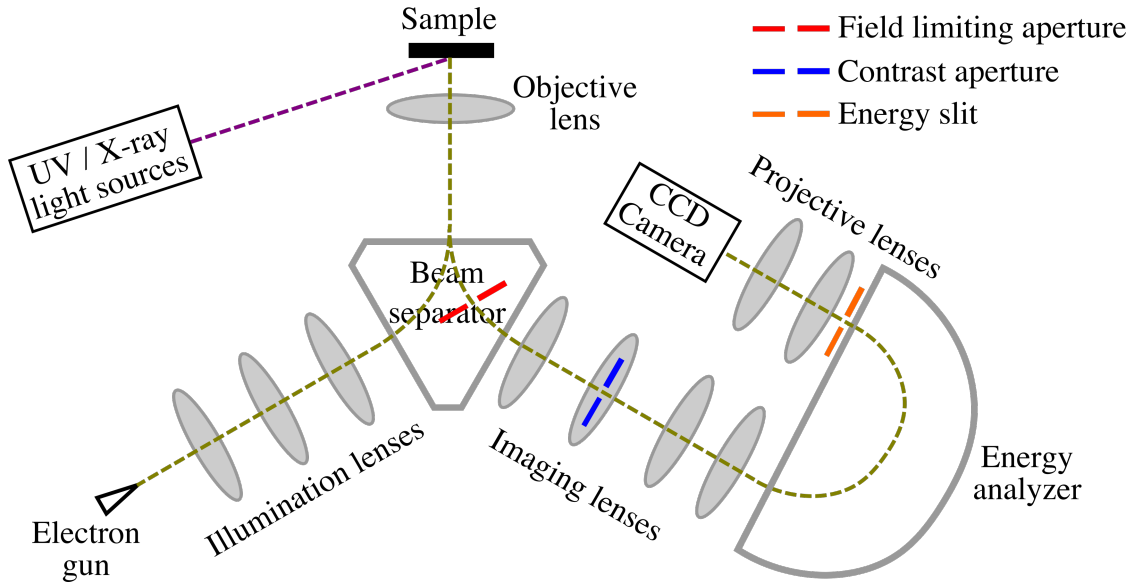
Figure 2.3: Schematic of a spectroscopic photoemission and low energy electron microscope

two factors that typically determine the overall resolution and the transmission of the system. The angle-limiting aperture, also known as the contract aperture is located at the diffraction plane after the beam separator. The introduction of the contrast aperture by Boersch in 1942 [13] aids in reducing the spherical and chromatic aberrations of the objective lens and thus achieving better resolution by transmitting only near incidence photoelectrons.

By tuning its focal plane, the intermediate lens places either the image plane or the diffraction plane at the entrance of the energy analyzer thus allowing PEEM to switch between real space or reciprocal space imaging. The energy analyzer together with an energy-selection slit placed at its exit, determines the energy resolution of the system, which is nowadays achievable in the ∼100meV range [18]. The projective lens then magnifies the image or the diffraction plane at the exit of the analyzer onto a detector that is made up of a microchannel plate, a fluorescent screen and a CCD camera. As the emitted photoelectrons are accelerated to high energy, all the lenses used are either electrostatic or magnetic lenses instead of optical lenses. Similar to the imperfection in the physical shape of an optical lens, electron lenses also suffer from astigmatism. As such, stigmators

and deflectors are incorporated into the imaging column to correct for such irregularities.

2.2.3   Light sources for PEEM

Gas discharge lamps

The first PEEM setup by Brüche in the 1930s came years before the first functional laser was built in the 1960s. Back then, mercury lamp fluorescence provides the necessary photons for PEEM applications. However, the wide energy distribution of the mercury lamp greatly limits the resolution of the microscope, rendering PEEM unable to compete with the thermionic emission electron microscope that had successfully surpassed the resolution of light microscope in 1942 [14]. This limitation is eventually overcome with the advent of two additional light sources for PEEM i.e. synchrotron radiation and frequency-multiplied laser source.

Synchrotron radiation

As a relativistic electron travels in a circular trajectory, it experiences a radial acceleration and emits an electromagnetic wave tangent to its trajectory. In a synchrotron facility, magnetic structures such as bending magnets, wigglers and undulators are used to accelerate electrons in a curved path for the generation of a wide spectrum of electromagnetic waves with high brilliance. Today's synchrotron facilities typically cover the electromagnetic spectrum from the extreme ultraviolet (EUV) to the hard x-ray regimes and are capable of generating high brilliance beam with an average brightness of $10^{20} photons/s/mrad^2/mm^2/0.1\%BW$ [19]. The wide spectral range and the high photon flux make synchrotron radiation a strong candidate for PEEM imaging. In addition, the new generation of synchrotrons is now capable of producing femtosecond pulses, adding high temporal resolution to PEEM imaging. However, such capability is still limited to only a handful of facilities. Furthermore, synchrotron facilities are generally large-scale operations with high overhead cost, are space-consuming, and are typically shared by

multiple research groups worldwide thus limiting beam time accessibility.

Table-top frequency-multiplied laser source

Frequency-multiplied laser source, on the other hand, is laboratory-based and thus has smaller footprint, significantly lower operation cost, and much less conflict over beam time availability. To date, many of the femtosecond lasers found in laboratory settings utilize titanium-doped sapphire (Ti:sa) crystal as their gain medium due to its wide gain bandwidth that allows for the generation of ultrashort pulses. These Ti:sa lasers have a wide range of wavelength tunability ranging from 1100nm to 650nm that is equivalent to the photon energy range of approximately $1-2$eV. This energy range is considerably low for the photoemission of electrons from most materials whose work functions typically lie within the range of $4-6$eV. Conveniently, the high intensity achievable by femtosecond lasers allows for the generation of light with higher photon energy through nonlinear frequency conversion processes.

There are two mechanisms for the generation of higher frequency light. One of the mechanisms is via nonlinear frequency conversion in nonlinear crystals. Nonlinear crystals are materials that exhibit strong nonlinear polarization response to the electric field of the driving laser as described by the following equation:

$$\mathbf{P}(t) = \varepsilon_0\chi^{(1)}\mathbf{E}(t) + \varepsilon_0\chi^{(2)}\mathbf{E}^2(t) + \varepsilon_0\chi^{(3)}\mathbf{E}^3(t) + ... \tag{2.2}$$

Materials with high $\chi^{(2)}$ nonlinearity are often used for nonlinear frequency conversion processes such as second harmonic generation and sum frequency generation. Beta barium borate (BBO) is one of these nonlinear crystals that possesses the required high $\chi^{(2)}$ coefficient and is widely used for the generation of the second, third and fourth harmonics of Ti:sa lasers. This mechanism is comparatively easy to implement and offers high conversion efficiency e.g. 40% conversion efficiency for the second harmonic generation of 800nm with a BBO crystal. The high conversion efficiency allows for the generation
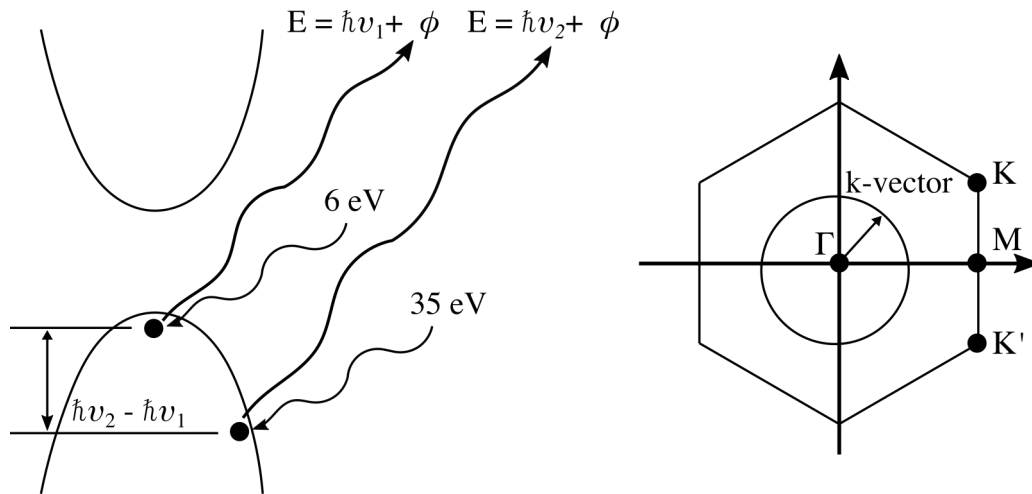
Figure 2.4: Band structure & Brillouin zone The schematic illustrates PEEM's access to different parts of the band structure and the Brillouin zone of a sample depending on the incident photon energy.

of higher frequency light with sufficient photon flux even at MHz repetition rate. The use of a high repetition rate light source minimizes space charge effect in the imaging column and allows for shorter image acquisition time for PEEM measurements. On the flip side, the main drawback of this mechanism is the transparency limit of the BBO crystal that is ∼190nm (6.5eV), below which the crystal becomes highly absorptive. The low photon energy, barely higher than the work functions of most materials, limits the access of PEEM to electrons from the upper part of the valence band as well as from within a small region of the Brillouin zone centering around the Γ point, as illustrated in Figure 2.4.

The second mechanism for generating higher harmonic orders of the fundamental laser frequency is via nonlinear interaction of an inert monatomic gas with an intense laser field of the magnitude of $10^{13} - 10^{15}$ W/cm^2. The energy of the photons generated is typically much higher than the work function, ϕ, of most materials and thus is capable of photoemitting electrons from deeper within the band structure (Figure 2.4). Furthermore, the k-space that can be imaged with these photons could easily cover the entire Brillouin zone of most materials thus allowing the study of physical processes happening at the high k-vectors. The main drawback of this mechanism is its low conversion efficiency of

$10^{-3} - 10^{-6}$ that necessitates either a high power laser with an average power of $>$80W [20] or a sophisticated enhancement cavity [21] to attain reasonable photon flux at MHz repetition rate.

As the band gap of GaAs lies at the Γ point, the generation of high frequency light using nonlinear crystals is the preferred mechanism due to its simplicity. In addition, as we are only interested in the photoexcited electrons, low energy photon is preferred to avoid photoemitting the electrons from the valence band which could potentially overwhelmed the signal or lead to space charge effect.

2.3 Time-resolved photoemission electron microscopy

2.3.1 Bringing in time resolution through optical pump-probe technique

With the imaging probe pulse in place, the inclusion of an ultrafast pump pulse and a delay stage to provide for the pump-probe delays are the logical next step to bring in the desired temporal resolution to the PEEM measurements via a pump-probe setup. As described in the previous chapter, the time-delayed photoemission of the photoexcited electrons allows TR-PEEM to image directly the photocarrier spatiotemporal distributions with high resolutions. Using TR-PEEM, various plasmonic processes on nanostructured metallic surfaces as well as the transport and recombination of photocarriers on semiconducting surfaces have been investigated as discussed in further details below (Figure 2.5).

2.3.2 Previous studies with TR-PEEM

The potential of time-resolved imaging was first realized experimentally in 2005 for the study of surface plasmon dynamics in a nanostructured silver film [22]. The simultaneous spatiotemporal imaging has allowed Kubo et al. to observe the quantum interference of

Previous studies with TR-PEEM
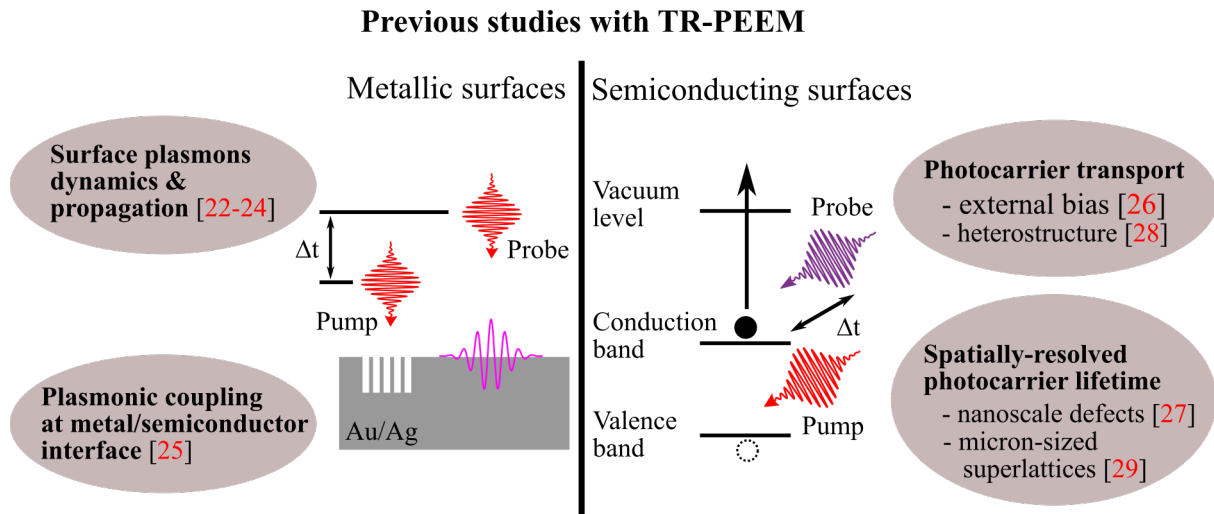
Figure 2.5: Previous studies with TR-PEEM. The schematic illustrates the use of TR-PEEM for the study of surface plasmons at metal/vacuum and metal/semiconductor interfaces as well as photocarrier transport and recombination in semiconductors.

the localized surface plasmons polarization waves [22]. Since then, this technique has enabled the study of coherent interaction between localized surface plasmons (SPs) and propagating surface plasmon polaritons (SPPs) [23], the imaging of SPPs propagation and interference at their native wavelength [24], and the understanding of the mechanism of hot electron generation at the interfaces of metallic nanoparticles and a semiconducting substrate [25].

Apart from the studies of various plasmonic processes on metallic surfaces and nanostructures, the potential of TR-PEEM in imaging the photocarrier dynamics in semiconductors has also been successfully demonstrated in recent years [26, 27, 28, 29]. In contrast to metallic surfaces, imaging of semiconducting surfaces is inherently more challenging due to the higher material resistivity. For the generation of high energy photon to overcome the material work function (typically $4 - 6$eV), a kHz amplifier system is generally preferred to attain sufficient photon flux of the 3rd and 4th harmonics. However, the use of a kHz system is also likely to result in a local buildup of the space charge as well as sample charging due to the higher number of photoemitted electrons per pulse and the higher material resistivity. On the other hand, though the use of a 80MHz oscillator

system minimizes the space charge effect and leads to better signal-to-noise ratio, the pulse energy is typically too low to generate sufficient flux of the high energy photons. By careful optimization of the laser pulse fluence and repetition rate, Fukumoto et al. demonstrated in 2014 the capability of TR-PEEM to image the photocarrier transport [26] and nanoscale defect recombination [27] on a semiconducting surface. Since then, TR-PEEM has been used to study the generation and transport of photoexcited electrons in a InSe/GaAs heterostructure [28] and to measure the lifetimes of micron-sized twisted graphene superlattices [29].

2.4 Chapter conclusion

The first part of this chapter described the main components of a spectroscopic photoemission and low energy electron microscope. It then went on to discuss the advantages and disadvantages of the different light sources available for the photoemission electron microscope. The second part of the chapter briefly discussed about the additional challenges in using TR-PEEM to image semiconducting surfaces. In contrast to metallic surfaces, semiconductors typically have higher sample resistivity which could result in sample charging as well as space charge effect. Hence, careful balancing of the need for high repetition rate system and the need for high pulse energy is critical for TR-PEEM imaging of semiconducting samples. The next chapter will describe in further details the optical layout of the pump-probe setup, its coupling into the PEEM measurement chamber as well as the preparation and characterization of the GaAs sample.

Chapter 3

Experimental setup & sample preparation

3.1   Chapter overview

As mentioned in the previous chapter, time-resolved photoemission electron microscopy (TR-PEEM) is a technique that combines the femtosecond temporal resolution of an ultrafast pump-probe spectroscopy with the nanoscale spatial resolution of a photoemission electron microscopy. The first part of this chapter will describe the optical layout of the ultrafast pump-probe setup as well as its operation together with the photoemission electron microscope. The second part of this chapter will cover the preparation and characterization of the sample to ensure a pristine surface. Some additional optical and electronic properties of the sample that are pertinent to the understanding of the experimental results will also be discussed here.

3.2   TR-PEEM optical layout

The laser system i.e. $FEMTOSOURCE^{TM}\ scientific^{TM}$ XL is a high energy Ti:sapphire oscillator system. XL runs at a repetition rate of 4MHz with pulse energy of 650nJ and

outputs 45fs pulses at a central wavelength of 800nm. As shown in Figure 3.1 , the 800nm output beam is split into two paths i.e. the pump and the probe paths, via the use of a half wave plate and a polarizing beam splitter. The 800nm pump beam is directed towards PEEM while the probe beam is directed towards a third and fourth harmonic generation setup (dashed box in Figure 3.1) for the generation of $4 - 6$eV photon energy. A motorized linear delay stage in the pump beam path provides the time delay between the arrival of the pump and the probe pulses at the sample.

The new 3rd and 4th harmonic generation setup (originally built by Vivek Pareek) follows the generation scheme as demonstrated in [30] and utilizes achromatic lenses to achieve a much better (circular) spatial beam profile, a higher conversion efficiency for the harmonic generation, and easier day-to-day alignment than the previous setup used in [28]. For the harmonic generation, the 800nm probe beam is first split into two paths: one to be used as a fresh 800nm beam for the 4th harmonic generation later while the other is used for the generation of both the 2nd and the 3rd harmonics. For the 2nd harmonic generation (SHG), the 800nm beam is focused tightly onto a 1.5mm thick BBO crystal ($\theta = 29.2°$, $\phi = 90°$) with a NIR coated (750nm – 1550nm), 40mm focal length achromatic lens to reduce chromatic aberration and hence achieve a shorter pulse width at the SHG crystal. In contrast to [30], BBO is chosen over a lithium triborate (LBO) crystal for its higher non-linearity. Both the generated 400nm and the remaining non-converted 800nm are then recollimated with a broadband UV-VIS coated (345nm – 700nm), 40mm focal length achromatic lens. All the achromatic lenses and the BBO crystals used for the harmonic generation are mounted on single-axis translation stages for precise control of the focusing and recollimation of the beam.

For the sum-frequency generation of the 3rd harmonic, the now perpendicularly polarized 400nm and 800nm beams are separated with a dichroic mirror. The 800nm beam that is not converted to 400nm is again reused for the generation of the 3rd harmonic. The 800nm beam goes through a delay stage for matching of the optical path while the 400nm is rotated with a half wave plate to match the polarization of the 800nm beam.
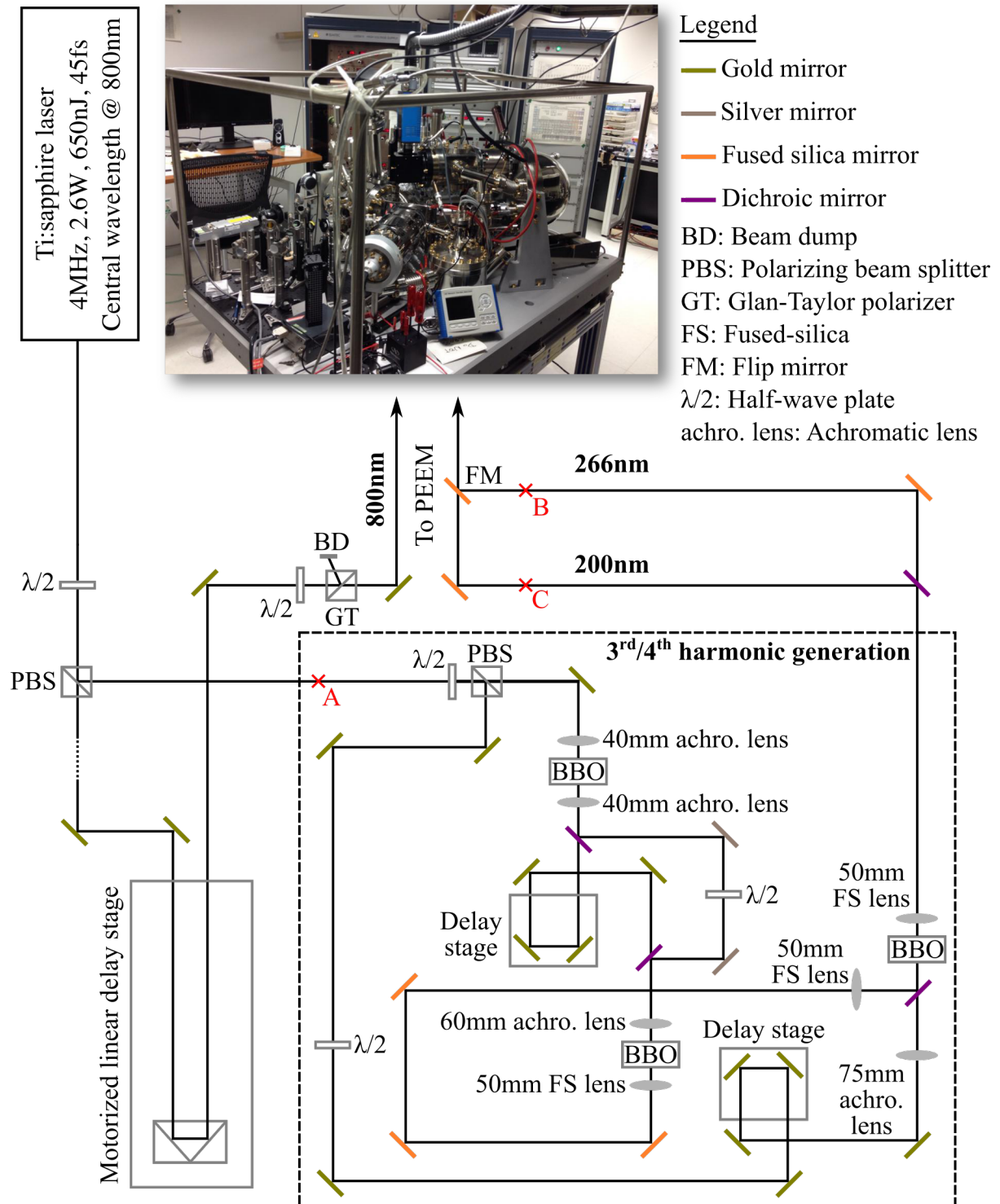
Figure 3.1: Schematic of the ultrafast pump-probe setup for TR-PEEM measurement

Both the beams are then recombined with a dichroic mirror and focused collinearly onto a 300μm thick BBO crystal ($\theta = 44.3°$, $\phi = 90°$) via a UV-VIS coated, 60mm focal length achromatic lens. Due to the transparency limit of the achromatic lenses, an uncoated UV grade fused silica lens with high transmission for the wavelength range of 200nm – 2μm is used to recollimate the generated 3rd harmonic i.e. 266nm beam.

Unlike the generation of the 3rd harmonic, a fresh 800nm beam with undisturbed intensity profile and pulse duration is used for the optical sum-frequency generation of the 4th harmonic. In addition, due to the lack of suitable achromatic lens that covers both the 266nm and the 800nm beams, the focusing of the beams are done non-collinearly. Both the 266nm and the fresh 800nm beam are combined with a dichroic mirror and focused onto a 100μm thick BBO crystal ($\theta = 65°$, $\phi = 90°$). A 50mm focal length UV fused silica lens mounted on a single-axis translation stage is placed after the BBO for recollimation of either the 266nm or the 200nm beam. For an incoming 800nm beam with an average power of ~500mW (measured at position A), the average power of 266nm and 200nm measured at position B and C after a dispersive prism, is approximately 5 – 10mW and $200 - 500\mu$W respectively.

As described in Chapter 2, the PEEM component of TR-PEEM is a SPELEEM from Elmitec. The SPELEEM microscope allows for both LEEM and PEEM imaging. The microscope is capable of high lateral resolution of better than 8nm in LEEM mode, and ~40nm in PEEM mode and an energy resolution of better than 115meV [31]. The sample mount is a 5-axis stage that allows for x, y and z translational motion as well as rotation around the z-axis i.e. θ_x and θ_y. The microscope main chamber connects with a preparation chamber allowing for additional sample preparation under ultrahigh vacuum at ~10^{-10}Torr, and a load lock chamber that allows for quick sample loading without having to vent the rest of the instrument to atmospheric pressure (Figure 3.2). Samples are transferred mechanically between the load lock chamber, the preparation chamber and the main chamber with a long sample transfer device. For the studies in this thesis, both the ultrafast pump and probe beams are coupled into the PEEM main chamber through
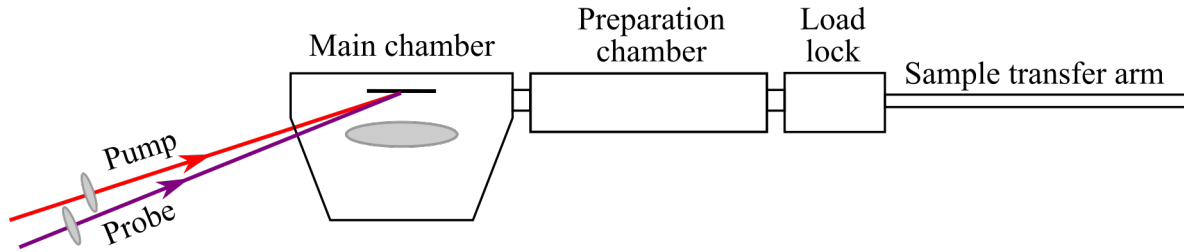
Figure 3.2: PEEM main measurement and auxiliary chambers. The red and violet lines illustrate the coupling of the pump and probe beams into the measurement chamber at a grazing angle of $\sim$18°.

a vacuum viewport at a grazing angle of $\sim$18°, as illustrated in Figure 3.2. The vacuum viewport is fitted with a UV grade fused silica window to allow for optimal transmission of the 266nm and 200nm probes.

3.3 Sample preparation & characterization

3.3.1 Sample preparation

The sample being studied is Zn-doped GaAs <100> wafer from Semiconductor Wafer Inc. The wafer is $350\pm25\mu$m thick and has a dopant concentration of $\sim10^{18}cm^{-3}$. The wafer was first cleaved into a 5x7mm sample and a short line was sculpted on the polished surface where the sample will be cleaved later in the ultrahigh vacuum to expose the <110> surface. The sample was then mounted onto the sample holder, loaded and transferred into the preparation chamber. There, the sample was heated to 150°C for at least an hour for the desorption of gases from the sample surface. After cooling, the sample was cleaved in-situ with the transfer arm to reveal the <110> surface and then transferred into the main chamber for measurements. The cleaved surface was confirmed with both low energy electron diffraction (LEED) (Figure 3.3A) and photoemission electron microscopy (PEEM) imaging (Figure 3.3B) to be pristine and free of microscopic ridges. A LEED pattern was measured both before and after the measurements to rule out significant surface changes over the course of measurements. All measurements were conducted at
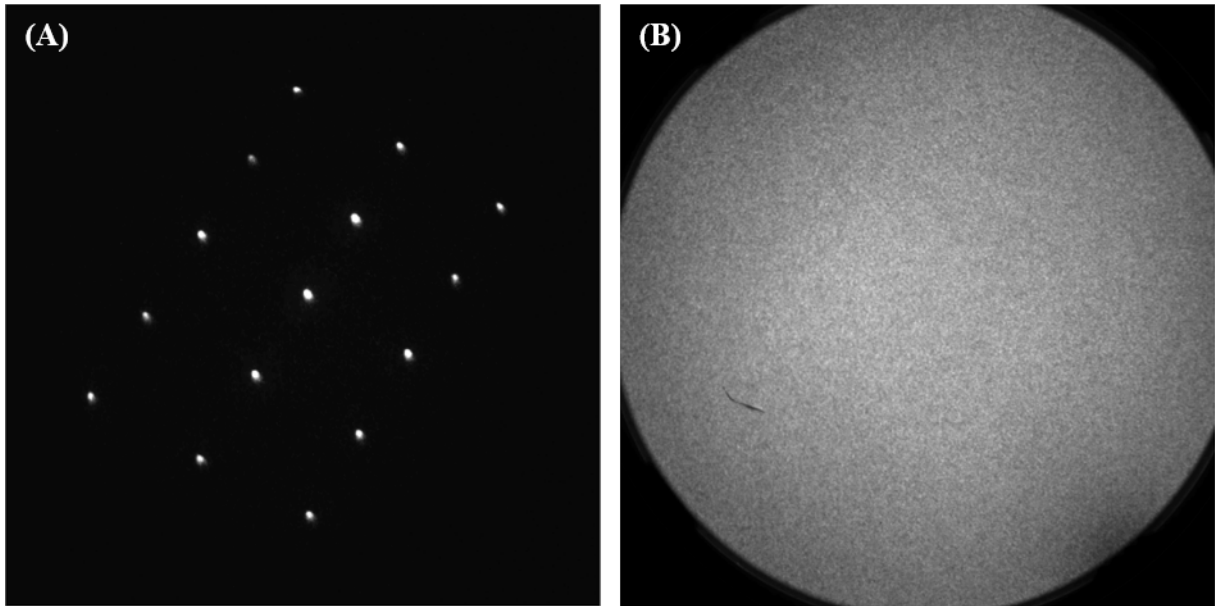
Figure 3.3: LEED & PEEM measurements of sample surface. (A) LEED pattern of the crystalline <110> surface measured at an electron energy of 32eV. (B) Photoemission of the sample surface with 266nm probe. The field-of-view is set to be 75μm. The hair-like artifact near the lower left region is not a feature on the sample surface but an artifact on the detector system.

least an hour after cleavage due to the alignment of the electron microscope and as such the band bending process as described in [32] was not observed.

3.3.2   Existence of surface states

The origin and nature of the surface states of GaAs <110> has been extensively investigated since 1970s [33, 34, 35, 36, 37, 38]. Although intrinsic surface states have been shown to be located outside of the band gap [39], mid-gap surface states have been known to occur due to cleavage defects [40] or gas adsorption on the sample surface [41]. In addition, by studying the surface band bending process of n- and p-type GaAs <110> surfaces immediately after in-situ cleavage, Deng et al. has proposed that the relaxation of the surface lattice after cleavage could also lead to the creation of surface states [32]. Irregardless of the origin, the existence of the mid-gap surface states will cause the carrier distribution in the band structure to change, resulting in the formation of a surface space

(A) Before equilibrium is achieved   **(B)** After equilibrium is achieved
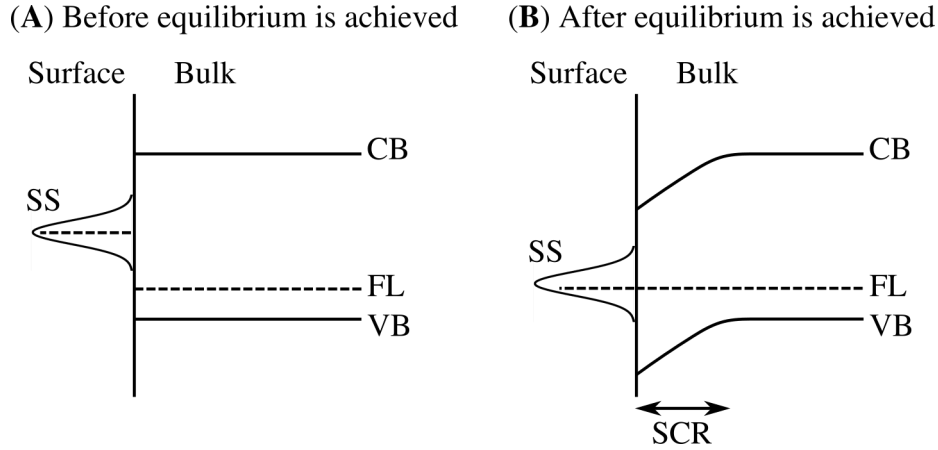
Figure 3.4: Surface bands bending in p-type GaAs. Band structures of p-type GaAs (A) before and (B) after equilibrium with the surface states is achieved. CB: conduction band, FL: fermi level, VB: valence band, SS: surface states, SCR: space charge region.

charge region and the bending of the surface bands as illustrated in Figure 3.4.

3.3.3   Optical penetration depth of the pump and probe pulses

For the dopant concentration of $10^{18} cm^{-3}$, the depletion width of the space charge region, w, extends $\sim$32nm beneath the surface according to the following equation [42]:

$$w = \sqrt{\frac{2\varepsilon_0 \varepsilon_r \Phi_b}{q N_d}} \tag{3.1}$$

where ε_0 is the vacuum permittivity, ε_r is the static relative permittivity, Φ_b is the band bending at the sample surface, q is the electron charge, and N_d is the dopant concentration. For the TR-PEEM measurement, both the pump and the probe beams are set to p-polarization with half wave plates placed right before the beams enter the main chamber of the microscope. The penetration depth of the 800nm pump is $\sim$700nm and that of the 266nm probe is $\sim$6nm [43, 44]. The narrow penetration depth of the probe compared to the depletion width allows TR-PEEM the capability to resolve the vertical transport of the photocarriers within the space charge region. Due to the large penetration depth of the 800nm pump, the gradient of the photoexcited carriers across the depletion width is
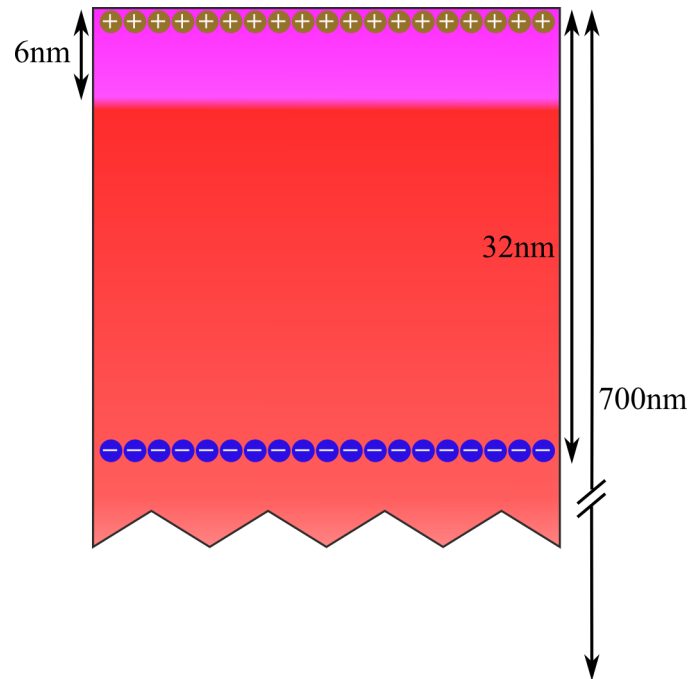
Figure 3.5: Schematic illustrating the extent of the optical penetration depths relative to the depletion width of the space charge region.

essentially constant.

3.3.4   Space charge effect

To demonstrate that the TR-PEEM measurements are not affected by any observable space charge effects due to the emitted photoelectrons, the photoemission spectrum for 266nm probe only is compared with the pump-probe photoemission spectra at the instant of photoexcitation i.e. at 0ps, for three different photoexcited carrier densities (Figure 3.6). The two peaks of the pump-probe spectra correspond to the surface states (lower energy) and the conduction band (higher energy) respectively. As the sample is hole-doped, very few electrons are photoemitted from the surface states at equilibrium. At 0ps, electrons are photoexcited from the valence band to both the surface states and the conduction band, resulting in a much higher photoemission signal from both states. At the photoexcited carrier density of 8.4 x $10^{18} cm^{-3}$, the integrated intensity shows approximately 100 times more photoelectrons detected than that with probe only (Figure
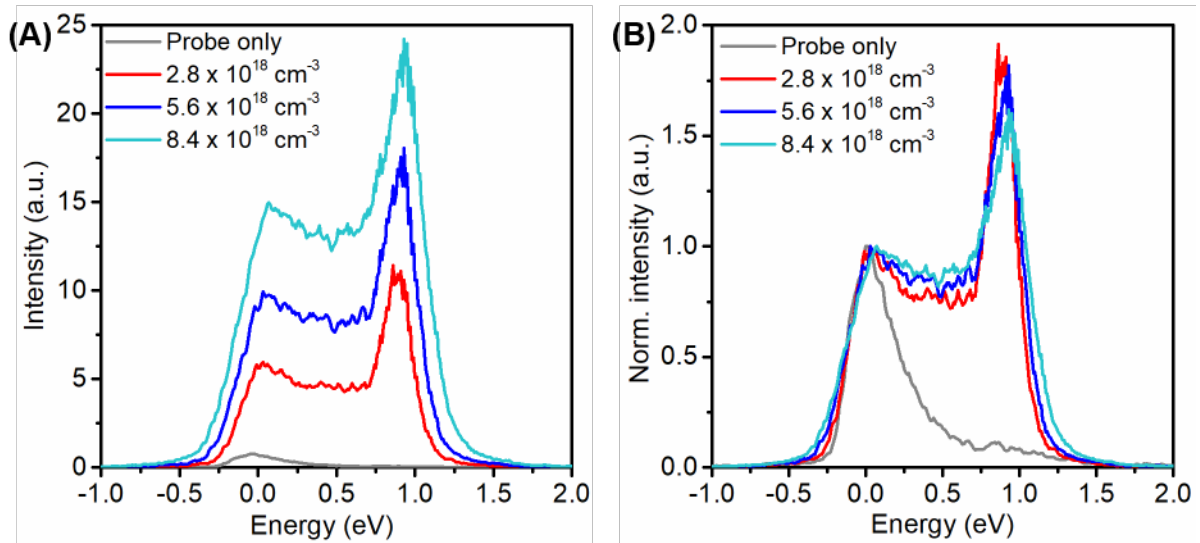
Figure 3.6: Photoemission spectra showing no observable space charge effect.
(A) Comparison of probe only photoemission spectrum with the pump-probe spectra at
0ps for three different carrier densities. (B) Normalized photoemission spectra to highlight
the absence of broadening of the spectra despite the large increase in the photoemitted
electron density.

3.6A). Despite the large increase in the emitted photoelectrons, there are no observable

broadening of the photoemission spectra (Figure 3.6B).

3.3.5   Confirmation of conduction band

The higher energy peak of the photoemission spectrum is confirmed to be the conduction

band by matching the band dispersion in a time-resolved angle-resolved photoemission

spectroscopy (TR-ARPES) measurement at 0ps (Figure 3.7). The white and red quadratic

lines each plot the energy-momentum dispersion relation i.e. $E(k) = E_0 + \frac{\hbar^2 k^2}{2m^*}$ with

the effective mass of $0.063m_0$ and m_0 respectively. The white line that plots the band

dispersion of the conduction band of GaAs matches well with the higher energy band in

the TR-ARPES measurement indicating it to be the conduction band. As the energy

separation between the two peaks in Figure 3.7 is ~1eV and the band gap of GaAs is

1.42eV, the lower peak is attributed to be the surface states. The red line plots the

instrument cut-off due to the energy of the probe photon.
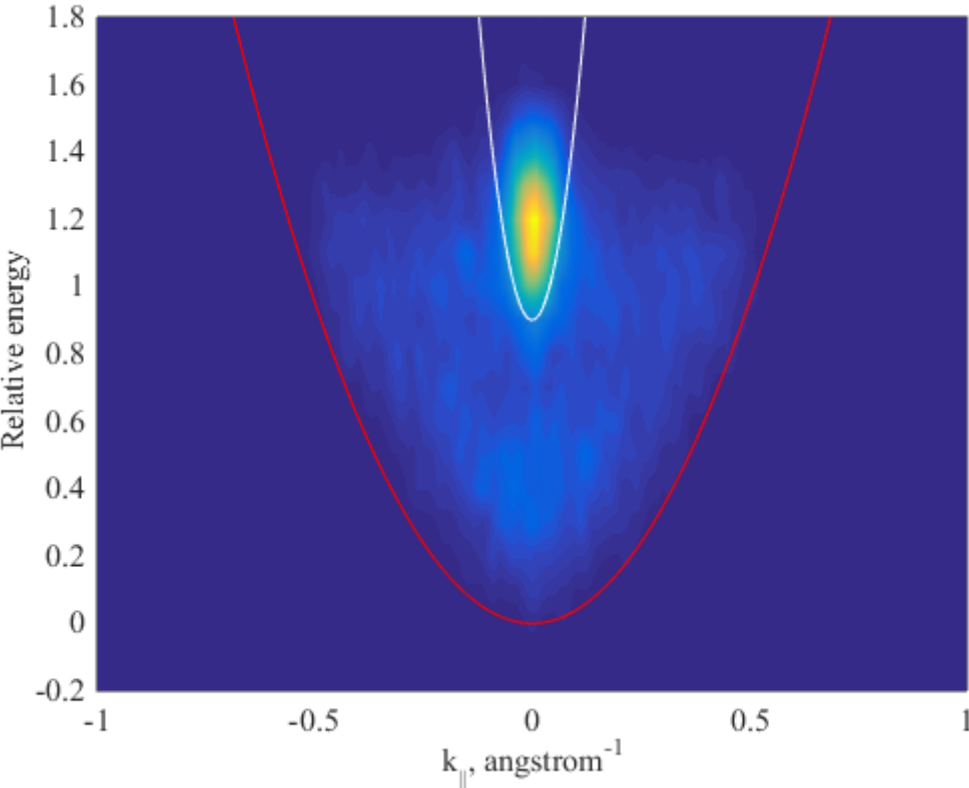
Figure 3.7: TR-ARPES of p-type GaAs <110> surface along the Γ-L direction at 0ps time delay

3.3.6   Beam spot size measurement

Contrary to conventional pump-probe measurement, the pump spot in TR-PEEM is set to be much smaller than the probe spot to ensure homogeneous photoemission of the photoexcited electrons. The probe spot size is hence set to be much larger than the 75μm field-of-view (FoV). The FWHM of the probe spot is determined using the knife-edge method to be approximately 370μm in diameter. Due to the grazing angle of incidence, the pump beam is elongated in one axis forming an elliptical photoexcitation spot on the sample (Figure 3.8A). The shorter axis of the elliptical photoexcitation spot is set to be smaller than the FoV and can be accurately determined from the photoemission spatial profile. To measure the FWHM of the photoexcitation spot, we first established that the integrated photoemission intensity varies linearly with the pump power, as shown in Figure 3.8B. A line profile is then extracted along the short axis of the elliptical photoexcitation spot (as illustrated by the yellow line in Figure 3.8A) and fitted with a Gaussian function showing a FWHM of $\sim 30\mu$m (Figure 3.8C).

3.3.7   Temporal resolution of TR-PEEM

The temporal resolution of the TR-PEEM measurements is obtained from the rise time of the pump-probe signal measured at a 4μm x 4μm region at the center of the photoexcitation spot for a photoexcited carrier density of 1.1 x $10^{19} cm^{-3}$. The Gaussian fit of the rise time shows a FWHM of $\sim$280fs (Figure 3.9). The 800nm pump is measured before the microscope view port with an autocorrelator ($Femtometer^{TM}$) to be $\sim$50fs. The cross correlation of the pump and probe Gaussian pulses is another Gaussian with a FWHM pulse width of $\sqrt{\Delta t_{pump}^2 + \Delta t_{probe}^2}$ where Δt_{pump} and Δt_{probe} are the FWHM of the pump and probe Gaussian pulses respectively [45]. With the equation, the 266nm probe pulse width is calculated to be $\sim$275fs. The broad 266nm pulse width is due to the laser pulse dispersion pre-compensation being optimized for maximum conversion efficiency of the harmonics and not for achieving the shortest pulse durations.
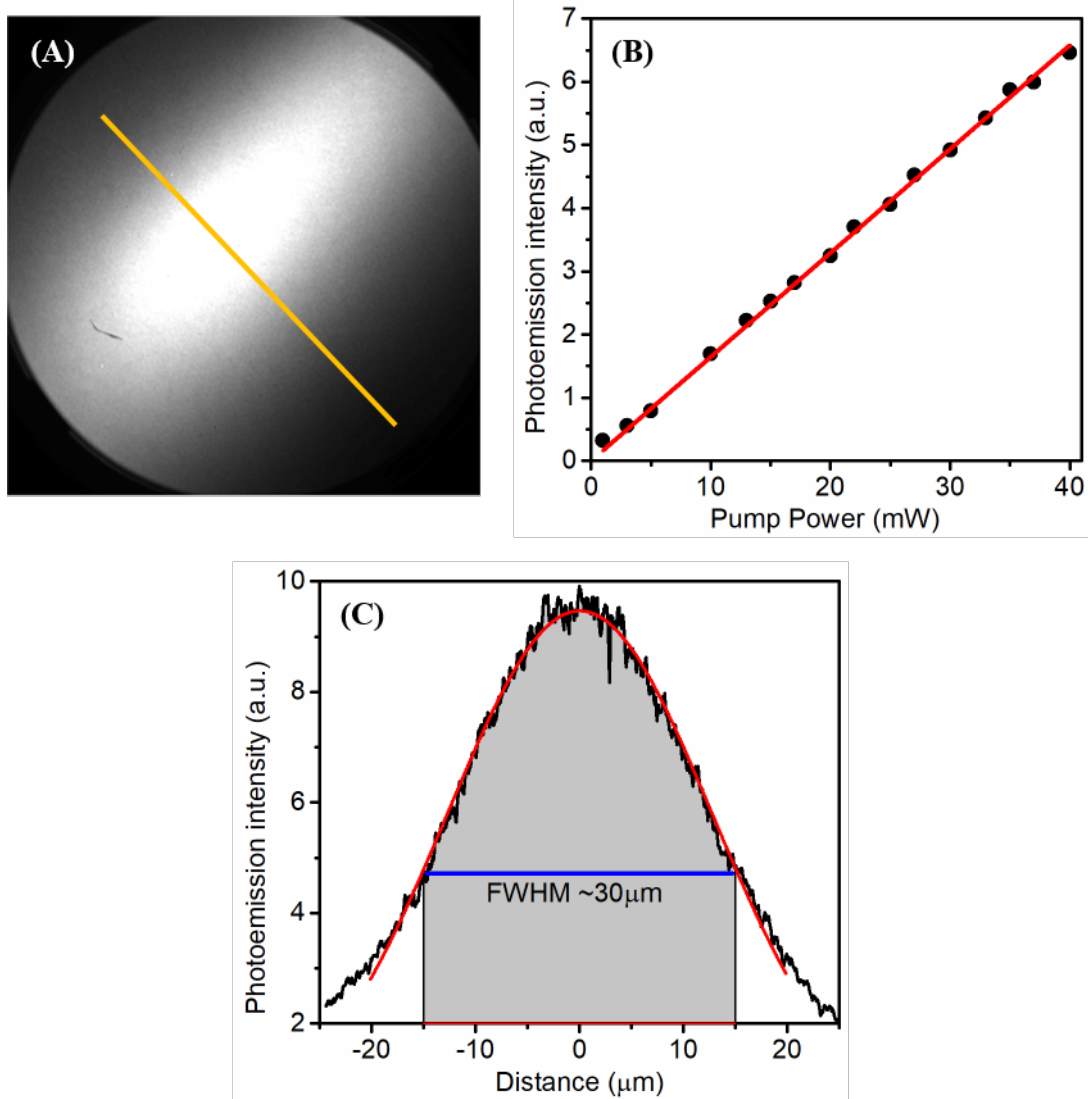
Figure 3.8: Determination of photoexcitation spot size. (A) TR-PEEM image of the elliptical photoexcitation spot at 0ps. The field-of-view of the microscope is set to 75μm. (B) Integrated photoemission intensity of the field-of-view as a function of the pump power. The red line shows a linear fit of the data points. (C) Line profile extracted along the short axis of the elliptical photoexcitation spot for pump power of 30mW, as illustrated by the yellow line in (A). The red line shows a Gaussian fit of the profile with a FWHM of $\sim$30μm.
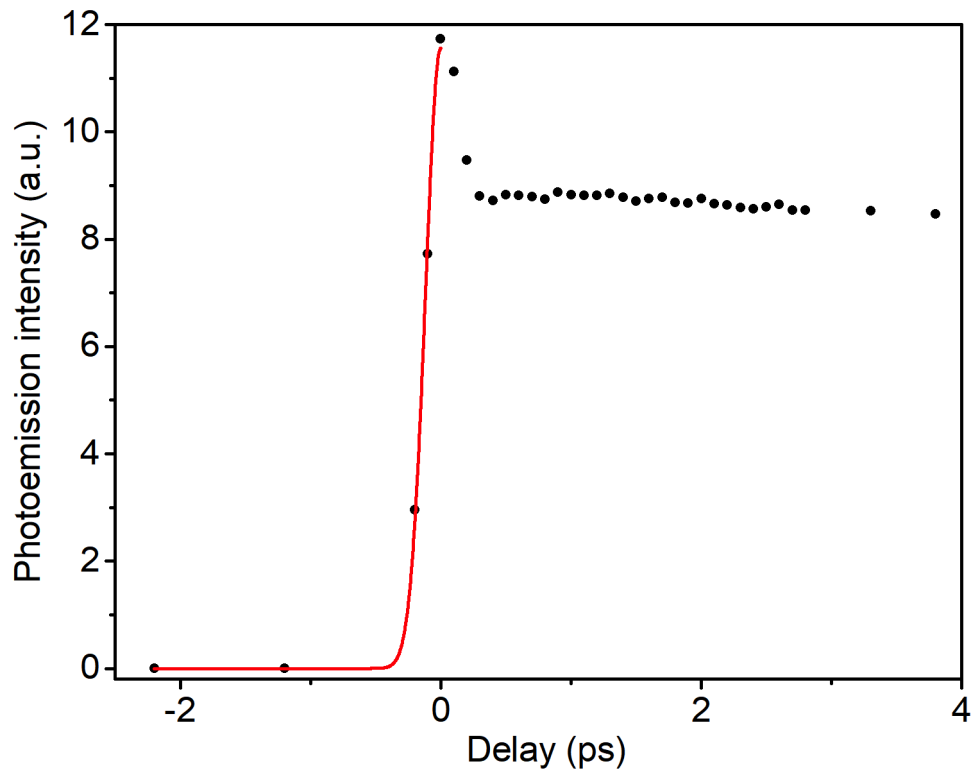
Figure 3.9: Determination of TR-PEEM setup temporal resolution. Time-delayed photoemission intensity at a photoexcited carrier density of 1.1 x $10^{19} cm^{-3}$. The temporal resolution of the TR-PEEM setup is estimated to be 280fs from the Gaussian fit (red solid line) of the rise time of the pump-probe signal (black data points).
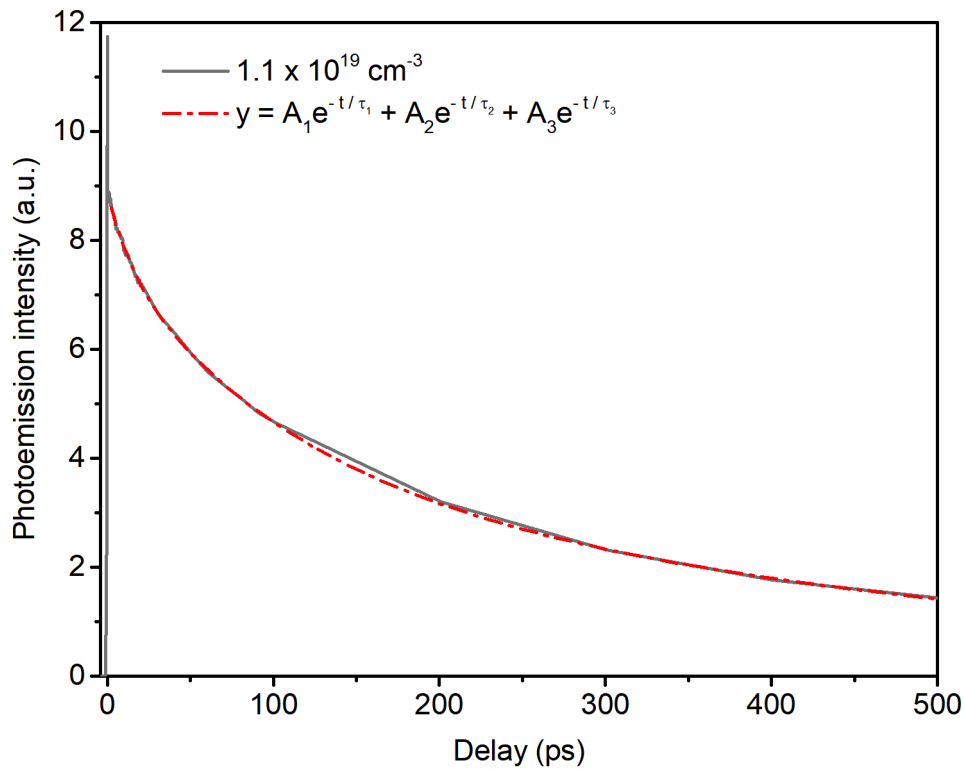
Figure 3.10: Determination of the photocarrier lifetime. An empirical tri-exponential fit of the pump-probe signal measured at a photoexcited carrier density of $1.1 \times 10^{19} cm^{-3}$. The fit shows a long-term decay time constant of $\sim$460ps.

3.3.8 Determination of photocarrier lifetime

To have an idea of the timescale at which the photoexcited carriers in the GaAs sample relax back to its equilibrium state i.e. pre-pump state, we fit the pump-probe curve measured at a photoexcited carrier density of $1.1 \times 10^{19} cm^{-3}$ with an empirical tri-exponential equation, as shown in Figure 3.10. The fit shows a long-term decay time constant of $\sim$460ps, denoting the timescale at which the photoexcited carriers relax back to its equilibrium state.

3.4 Chapter conclusion

The first part of this chapter described in detail the optical layout of the 3rd and 4th harmonic generation and the pump beam path. It then described the auxiliary chambers

connected to the main chamber of the electron microscope and the coupling of the pump and probe beams into the main chamber for measurements. The second part of this chapter described the preparation method for obtaining a pristine <110> surface of the Zn-doped GaAs sample. It then went on to discuss the origin and nature of the surface states at GaAs <110> surface and how the creation of the surface states leads to the bending of the surface bands and the buildup of an intrinsic surface space charge field. The width of the space charge region and the penetration depth of the ultrafast pulses are then calculated to showcase TR-PEEM capability to resolve the vertical transport of the photocarriers within the space charge region. The chapter then went on to compare the photoemission spectra of probe only with that of pump-probe measurements to verify that the TR-PEEM measurements are not affected by any observable space charge effect. The two peaks of the photoemission spectra are confirmed to be the surface states and the conduction band via matching the band dispersion in the TR-ARPES measurement. The chapter finished with the determination of the probe and the pump spot sizes as well as the temporal resolution of the TR-PEEM measurements to be $\sim 370 \mu$m, $\sim 30 \mu$m, and ~ 280fs respectively. The next chapter will discuss the control of the vertical transport of electrons to the sample surface at early time delays.

Chapter 4

Controlling the vertical transport of photocarriers

4.1   Chapter overview

This chapter studies the control of vertical transport of photoexcited electrons to the sample surface at early time delays. Using TR-PEEM, the chapter first describes the visualization of inhomogeneous photocarrier dynamics on a homogeneous p-type GaAs sample where a depletion in the electron population is observed at the center of the photoexcitation spot while a gain in the electron population is observed near the FWHM boundaries. The chapter then goes on to discuss the two competing intensity-dependent processes i.e. the vertical transport of photocarriers due to the intrinsic surface field and the many body Auger processes that lead to the observed spatial variation in the photocarrier dynamics. With this understanding, the chapter then demonstrates that the intensity profile of the photoexcitation beam can be utilized to control these processes. This is then followed by a discussion of how the inhomogeneous dynamics affects the electron distribution on the sample surface.

4.2   Experimental method

As described in Chapter 3, the sample being studied is a p-type GaAs cleaved in-situ to expose a pristine <110> surface (Figure 3.3). A 1.55eV pump pulse is used to photoexcite the electrons above band gap and a 4.65eV probe pulse is used to photoemit the photoexcited electrons. The photoemitted electrons are then collected by PEEM to form a series of time-delayed images reflecting the distribution of the photoexcited electrons both in space and in time. The narrow penetration depth of the probe pulse compared to the width of the depletion region has allowed PEEM the capability to resolve the vertical transport of the electrons to the sample surface. To study the local photocarrier dynamics as a function of the intensity variation within the photoexcitation beam, the pump spot size is set to be much smaller than the probe spot size to ensure homogeneous photoemission. Due to the dissimilar intensity gradient along the two axes of the elliptical photoexcitation spot (Figure 3.8A), the discussions in this chapter will focus on the variation in the local photocarrier dynamics along the short axis. Further details of the setup and the characterization of the sample are described in Chapter 3.

4.3   Inhomogeneity of physical processes within the full-width-half-maximum

Using TR-PEEM, the spatial distributions of the photoexcited electrons for three different photoexcited carrier densities are first imaged at a fixed time delay of +2.5ps (Figure 4.1A). The images are set to show the photocarrier dynamics within the FWHM of the short axis of the pump beam. Furthermore, to highlight the relative gain (red) or loss (blue) in the photoexcited electron density after the instant of photoexcitation, the images at +2.5ps delay are subtracted with their respective images at 0ps.

At low photoexcited carrier density ($2.8 \times 10^{18} cm^{-3}$), an increase in the photoexcited electron density is observed throughout the spot. The increase in the electron density af-
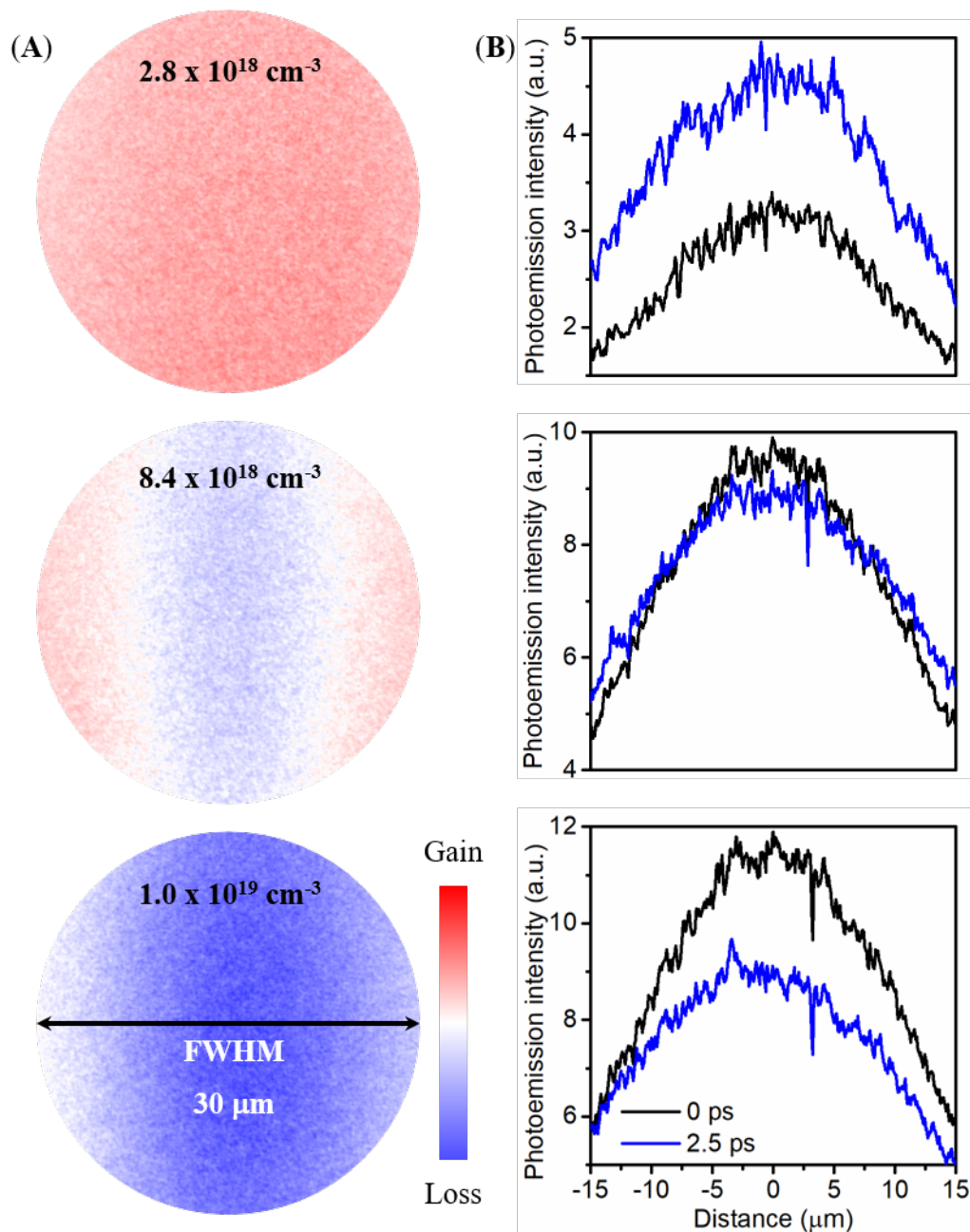
Figure 4.1: Spatial inhomogeneity in the photocarrier dynamics within the FWHM. (A) Spatial distribution of the photoexcited electrons within the FWHM of the short axis of the elliptical photoexcitation spot at a fixed time-delay of +2.5ps after photoexcitation. The images are subtracted with their respective images at 0ps to highlight the relative gain (red) or loss (blue) of electrons after photoexcitation. The images are rotated so that the axes of the pump spot are parallel to the x-y coordinates. (B) Spatial distribution profile of the electrons extracted along the short axis (as indicated by the black double-headed arrow in (A)) for both 0ps and +2.5ps time delays.

ter the instant of photoexcitation is a result of the vertical transport of the photoexcited electrons from the bulk to the sample surface due to the intrinsic surface space charge field (Figure 3.4). At high photoexcited carrier density (1.0 x $10^{19} cm^{-3}$), a general loss of the photoexcited electrons are observed throughout the spot. The depletion in the electron density is attributed to Auger recombination as discussed in the next section. In contrast to the general gain and loss of electrons observed at both the low and high photoexcited carrier densities, an intriguing spatial variation is observed at the intermediate photoexcited carrier density (8.4 x $10^{18} cm^{-3}$) – depletion of electrons is observed near the center of the photoexcited spot while an accumulation of electrons is observed further away from the center.

For quantitative comparison, the photoemission intensity profiles along the FWHM (as indicated by the double-headed arrow in Figure 4.1A) for both 0ps and +2.5ps delays are extracted (Figure 4.1B). As demonstrated by the images, the photoemission intensity profiles show a general increase across the spot at low carrier density and a general decrease at high carrier density. At intermediate carrier density, the intensity profiles clearly show the contrasting photocarrier dynamics with a decrease in the photoemission intensity at the center of the FWHM and an increase near the FWHM boundaries. In addition to the intriguing spatial variation observed, a fine-tuning of the carrier density around the intermediate range further shows that the relative sizes of the two regions with contrasting dynamics can be finely controlled, as demonstrated in Figure 4.2.

4.4 Verification of vertical transport and Auger recombination

To verify that the vertical transport of the excited photocarriers and Auger recombination indeed lead to the observed gain and loss of electrons, the time-delayed photoemission intensity at a small 4μm x 4μm region at the center of the photoexcited spot is measured as a function of the photoexcited carrier densities (Figure 4.3A). The small measure-
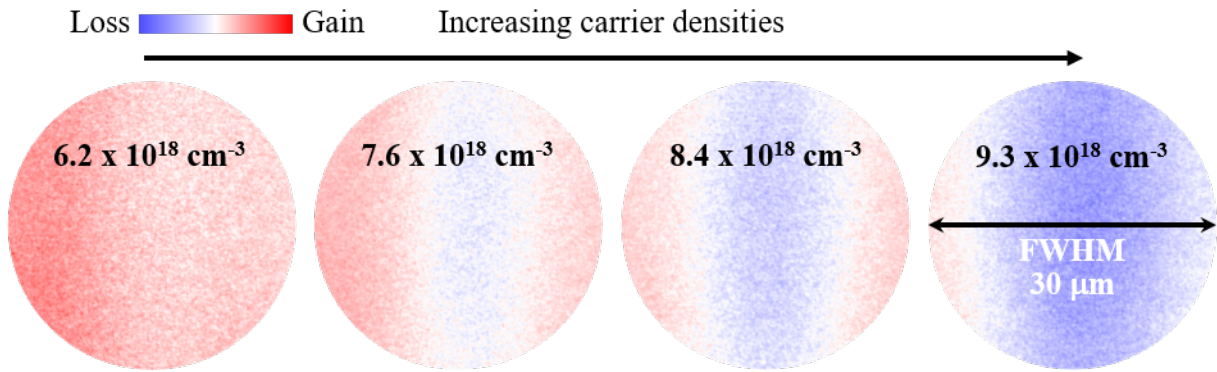
Figure 4.2: Controlling the relatives sizes of the two contrasting regions by fine-tuning the photoexcited carrier densities. The images are rotated with the axes of the elliptical photoexcitation spot parallel to the x-y coordinates for easy comparison.

ment region is chosen to ensure that the carrier dynamics is spatially averaged across an effectively constant photoexcitation intensity (Figure 4.3B–C).

For the low carrier densities, upon photoexcitation, the electrons drift towards the sample surface while the holes drift towards the bulk under the influence of the intrinsic surface field. This leads to an increase in the photoexcited electron density at the sample surface and hence the increase in the photoemission intensity (Figure 4.4A). The separation of the photoexcited electron-hole pair leads to the buildup of an opposite electric field that then partially screens the intrinsic surface field. As the carrier density increases, the partial screening of the intrinsic field becomes faster and more effective, resulting in reduced vertical transport of the photocarriers. A single exponential fit of the rise time of the pump-probe signals shows a decreasing trend from 3.5ps to 0.9ps (Table 4.1). At sufficiently high carrier density i.e. $9.8 \times 10^{18} cm^{-3}$ (Figure 4.3A), the intrinsic field becomes completely screened upon photoexcitation and no vertical transport of the photoexcited electrons is observed as evidenced by the lack of rise in the photoemission intensity. The signal instead decreases monotonously as the photocarriers decay and recombine over time. The observed screening dynamics as a function of the photoexcited carrier density (Figure 4.3A) agrees with previous literature [46].

In addition to the increasing partial screening of the intrinsic field, a rapid depletion
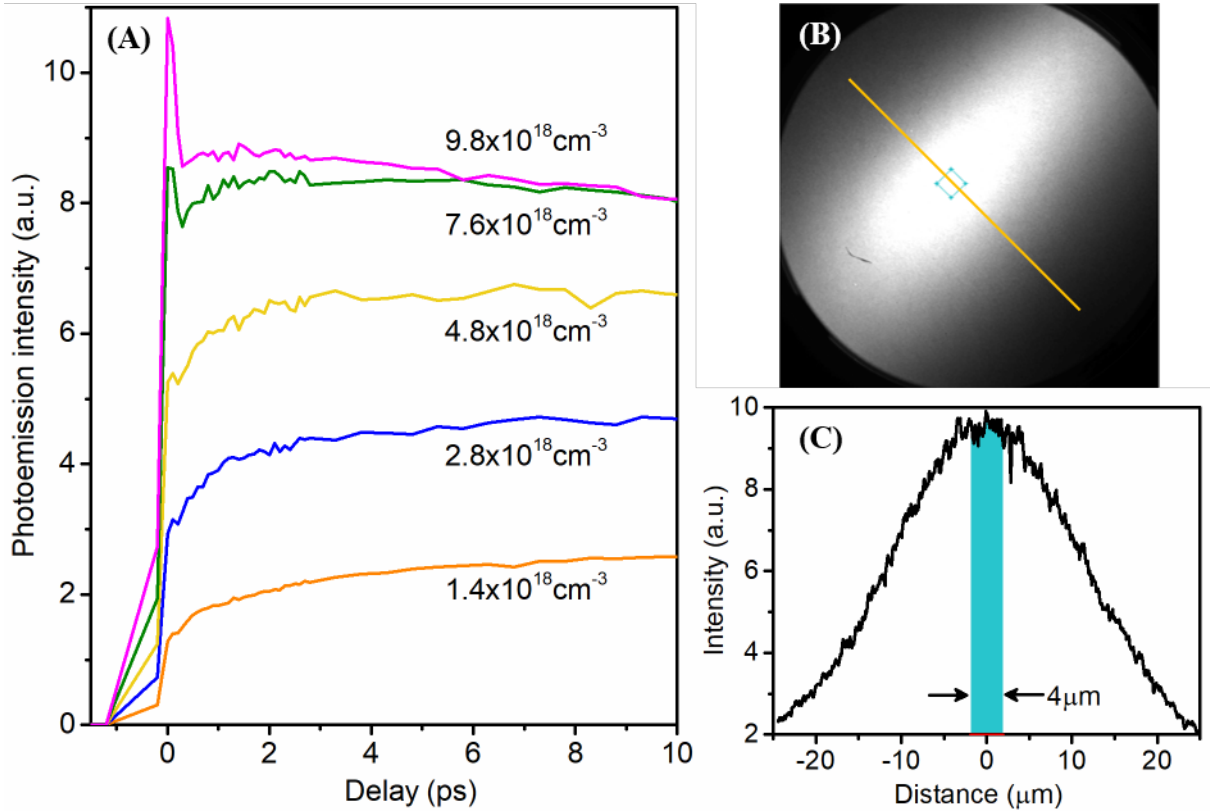
Figure 4.3: Screening dynamics of the photocarriers as a function of the photoexcited carrier density. (A) Local time-delayed photoemission intensity as a function of the photoexcited carrier densities. (B) TR-PEEM image at 0ps indicating the 4μm x 4μm measurement region at the center of the photoexcitation spot. (C) Photoemission intensity profile along the short axis of the photoexcitation spot (as indicated by the yellow line in (B)) showing the effectively constant intensity across the 4μm spot.

Table 4.1: Single exponential fit of the rise time of time-delayed photoemission signals for low carrier densities.

Photoexcited carrier density (cm^{-3})	2.8 x 10^{17}	1.4 x 10^{18}	2.8 x 10^{18}	4.8 x 10^{18}
Rise time (ps)	3.5	2.6	1.4	0.9
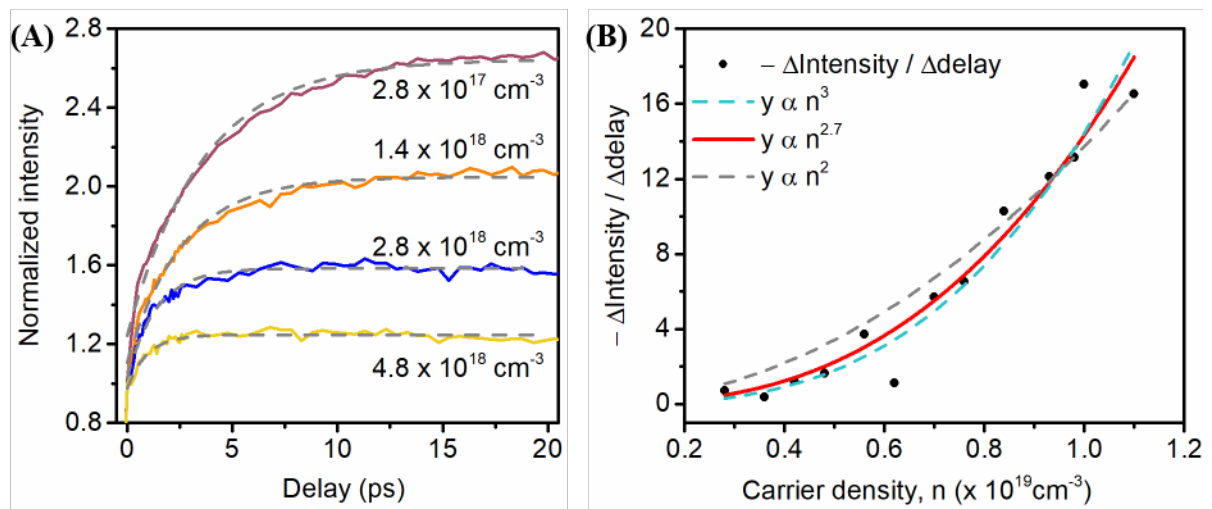
Figure 4.4: Photocarrier dynamics at low and high carrier densities. (A) Vertical transport of photoexcited electrons to the sample surface at low photoexcited carrier densities. The pump-probe signals are normalized to their respective intensities at 0ps to highlight the relative gain in the electron populations. The dotted grey lines are single-exponential fits of the pump-probe signals. (B) The rate of decrease in the photoemission intensity exhibits a power law dependence on the photoexcited carrier density i.e. $-\frac{\Delta Intensity}{\Delta delay} \propto n^{2.7}$. For comparison, both the quadratic and the cubic fits are also plotted showing better agreement of the rate of decrease to the cubic fit.

of the electron population within the first few hundreds of femtoseconds starts to emerge at high photoexcited carrier densities. To verify the origin of this sharp drop in the electron population, the rate of decrease in the photoemission intensity ($-\frac{\Delta Intensity}{\Delta delay}$) is plotted as a function of the photoexcited carrier density, n (Figure 4.4B). A power law fit shows that $-\frac{\Delta Intensity}{\Delta delay}$ is proportional to $n^{2.7}$, indicating the origin to be some sort of many-body effect. Both the quadratic and cubic fits are also plotted for comparison. The closer agreement of the data to the cubic fit suggests a stronger n^3 contribution, indicating Auger recombination to be the main contributor to the sharp peak observed at high carrier densities.

4.5 Controlling the spatiotemporal dynamics of photo-carriers

With an understanding of the local carrier dynamics happening at the center of the photoexcitation spot, this section now looks at the spatial variation in the carrier dynamics that arises due to the interplay between the two intensity-dependent processes for the intermediate carrier density of 8.4 x $10^{18} cm^{-3}$ (Figure 4.5A). Immediately after photoexcitation, at +0.3ps delay, a depletion in the electron population is observed in the entire spot. As the time delay increases, an influx of electrons starts to emerge near the FWHM boundaries while the electron population near the center of the spot continues to show a loss.

To understand the interplay between the two intensity-dependent processes, the time-delayed photoemission intensity at three spatial locations at varying distances from the center of the photoexcitation spot is plotted (Figure 4.5B–C). The measurement at the center is extracted from a 4μm x 4μm region similar to that described in the previous section. In contrast, the other two measurements are extracted from a 2μm x 4μm region in an effort to minimize the spatial averaging effect across the sharply decreasing slope of the Gaussian intensity profile (Figure 4.3C) while still maintaining reasonable signal-to-
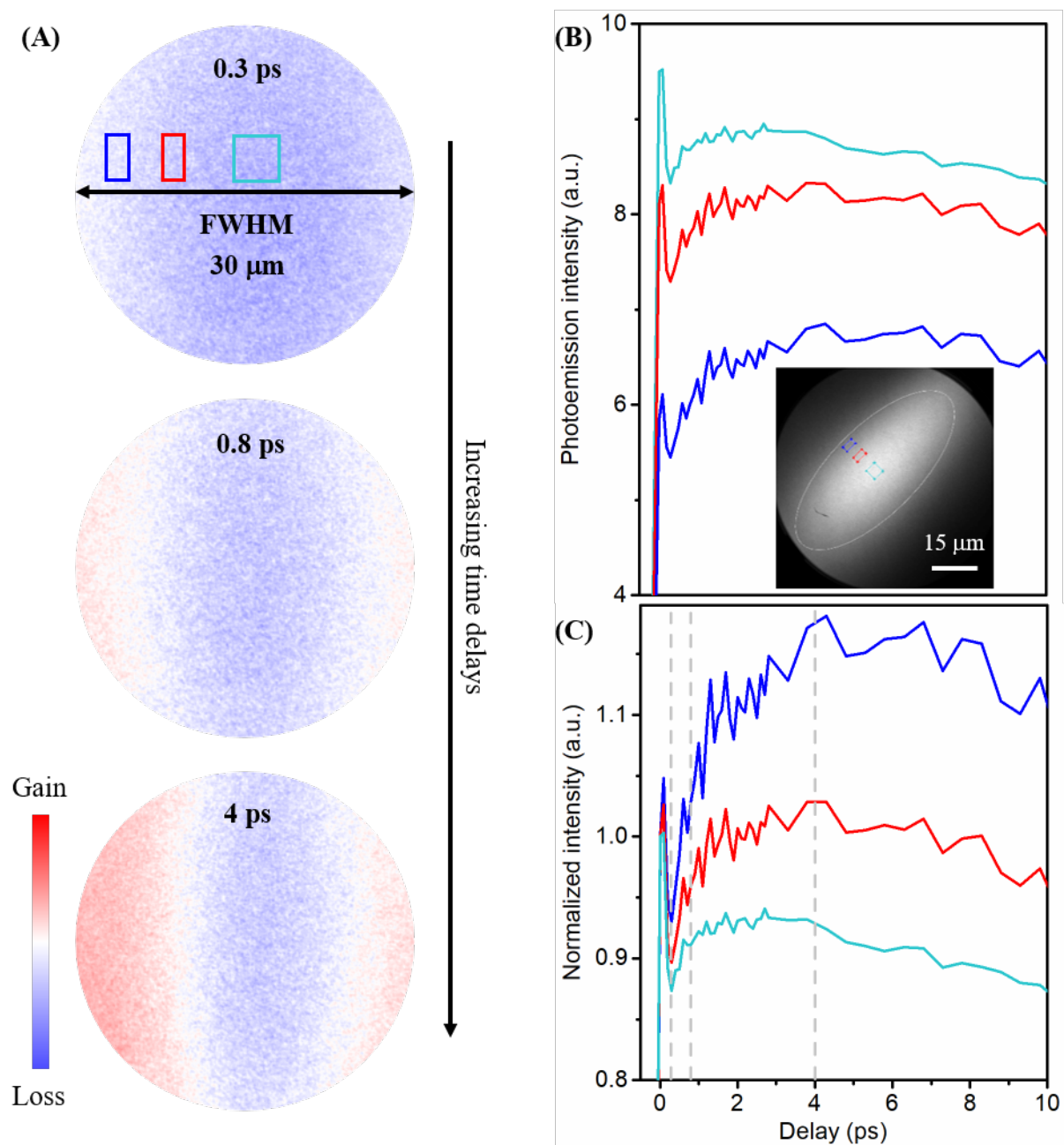
Figure 4.5: Spatial variation in the local carrier dynamics for the intermediate carrier density of 8.4 x 10^{18}cm^{-3}. (A) TR-PEEM images at three separate instances of time delays i.e. +0.3ps, +0.8ps and +4ps (grey dashed lines in (C)) showing the spatiotemporal evolution of the photoexcited electron density. The images are subtracted with the image at 0ps to highlight the relative gain (red) and loss (blue) in the local electron density. (B) Time-delayed photoemission intensity measured at three different spatial locations (indicated in inset) along the short axis of the pump spot. The white ellipse in the PEEM image (inset) marks the FWHM boundary of the elliptical pump spot. (C) The time-delayed photoemission intensities in (B) are normalized to their respective intensities at 0ps to highlight the relative gain and loss of electrons over time.

noise ratio.

Near the center of the photoexcitation spot, the relatively higher carrier density leads to stronger Auger recombination and minimal vertical transport of the photocarriers as the intrinsic field is almost completely screened. Further away from the center, the decreasing carrier density results in the weakening of the Auger process as well as the partial screening of the intrinsic field. As such, the gain in the electron population due to the decreasing partial screening starts to compensate for and eventually overtake the loss of electrons due to Auger recombination (Figure 4.5C). The different temporal characteristics for the two processes – fast Auger recombination occurring within few hundreds of femtoseconds, and slow vertical drift of the electrons occurring over a few picoseconds, lead to the observed spatiotemporal dynamics in Figure 4.5A. The fast Auger process initially dominates the entire region at 0.3ps while the vertical drift starts to emerge from the FWHM boundaries and grow inwards at later delays. Similar analysis at three other intermediate carrier densities are performed to demonstrate the capability to control the relative sizes of the regions where the two processes dominate (Figure 4.6 – 4.8).

4.6   Impact upon electron distribution profile

With the understanding that the intensity variation within the photoexciting pulse can be leveraged to control the spatially inhomogeneous carrier dynamics, this section now looks at how the inhomogeneity impacts the distribution of the photoexcited electrons on the sample surface over time. To observe the spatiotemporal evolution of the electron distribution, the photoemission intensity profile along the short axis of the photoexciting beam is extracted and fitted with a Gaussian function. The FWHM of the fitted Gaussian is then plotted as a function of the pump-probe temporal delay (Figure 4.9A–C, E).

Due to the loss of electrons at the center and the gain of electrons near the FWHM boundaries, the photoemission intensity profile for the intermediate carrier density of 7.6 x $10^{18} cm^{-3}$ shows a rapid broadening of approximately 7μm within the first 5ps after
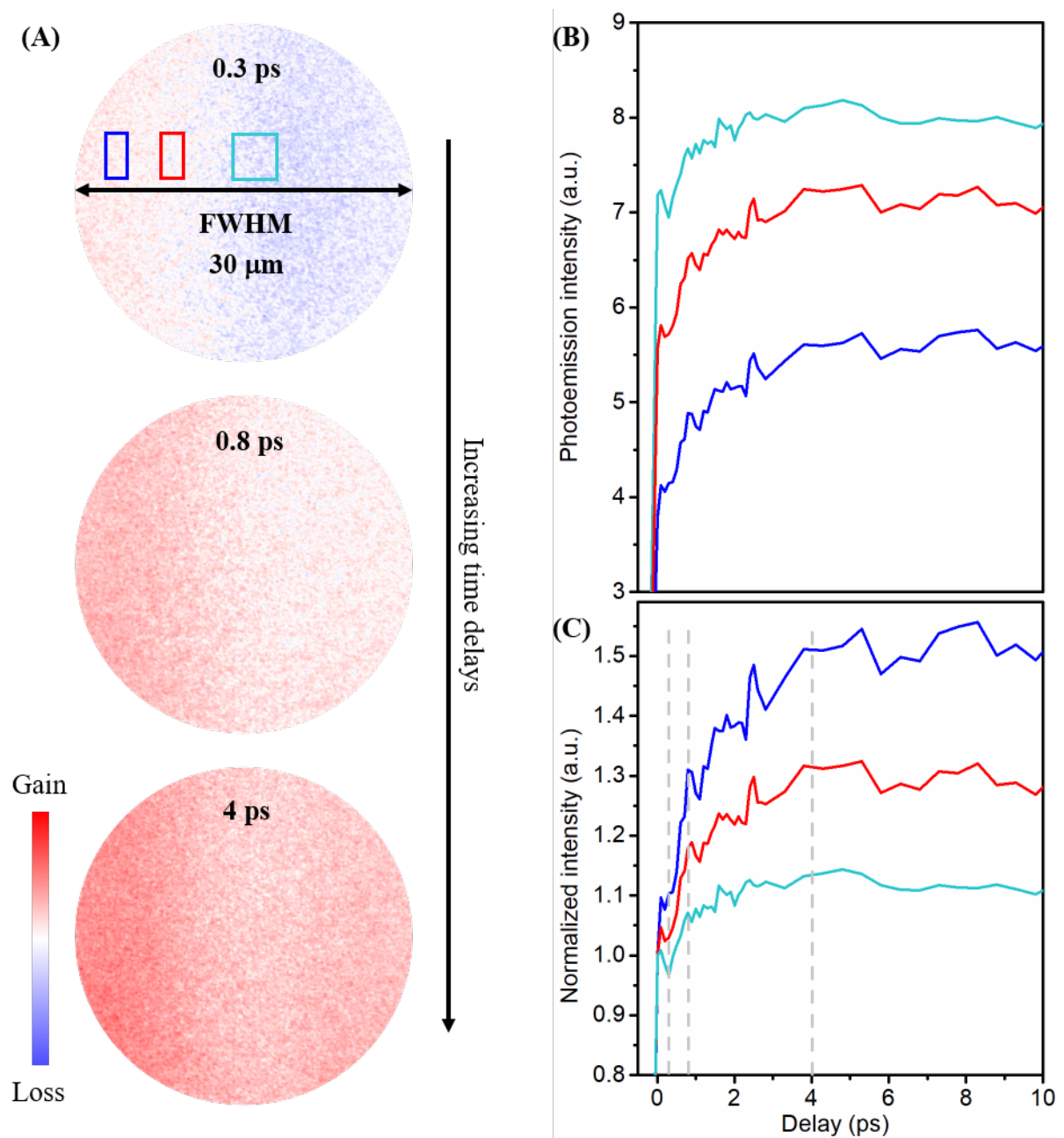
Figure 4.6: **Spatial variation in the local carrier dynamics for an intermediate carrier density of 6.2 x 10^{18}cm^{-3}.**
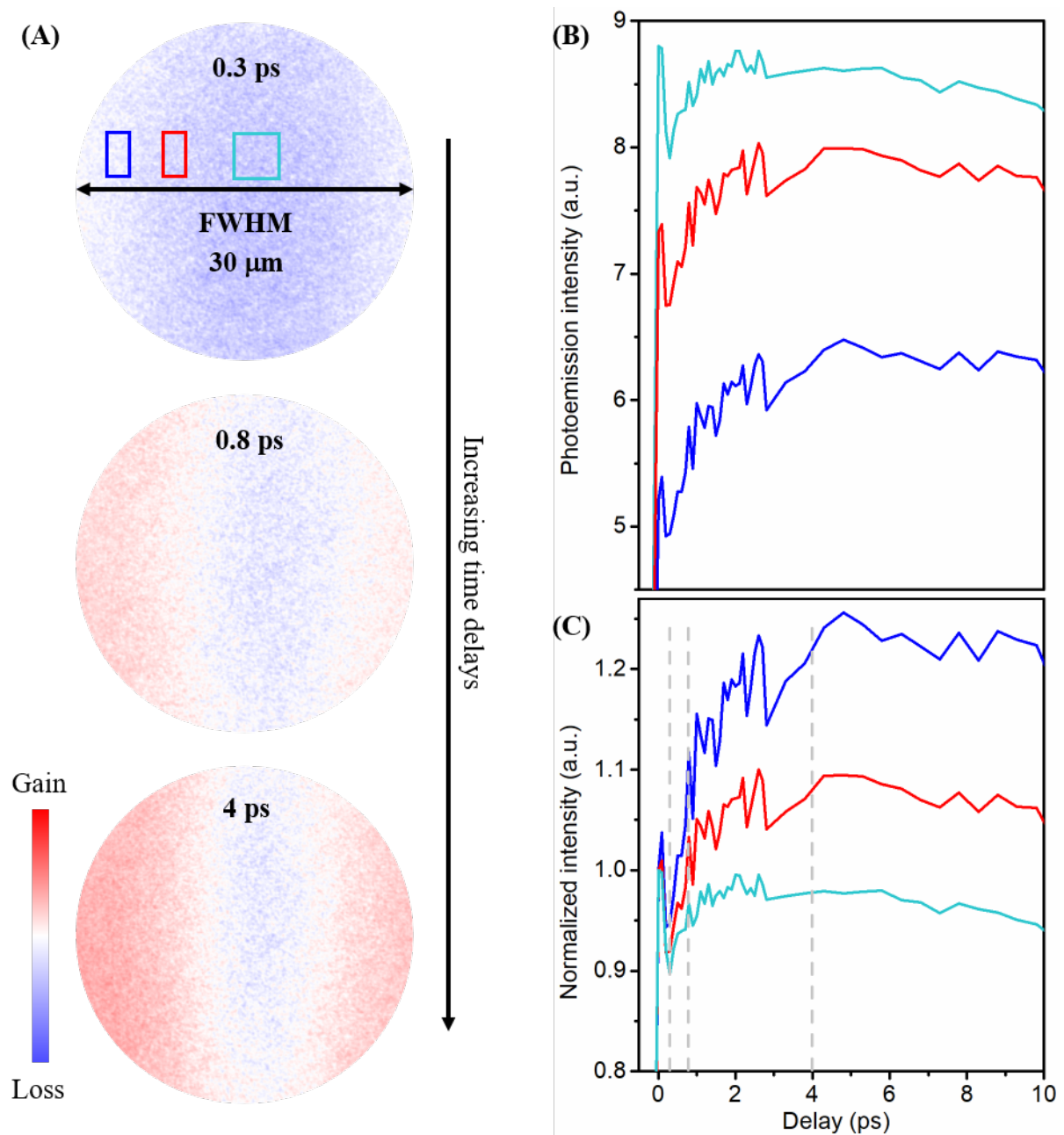
Figure 4.7: Spatial variation in the local carrier dynamics for an intermediate carrier density of 7.6 x 10^{18}cm^{-3}.
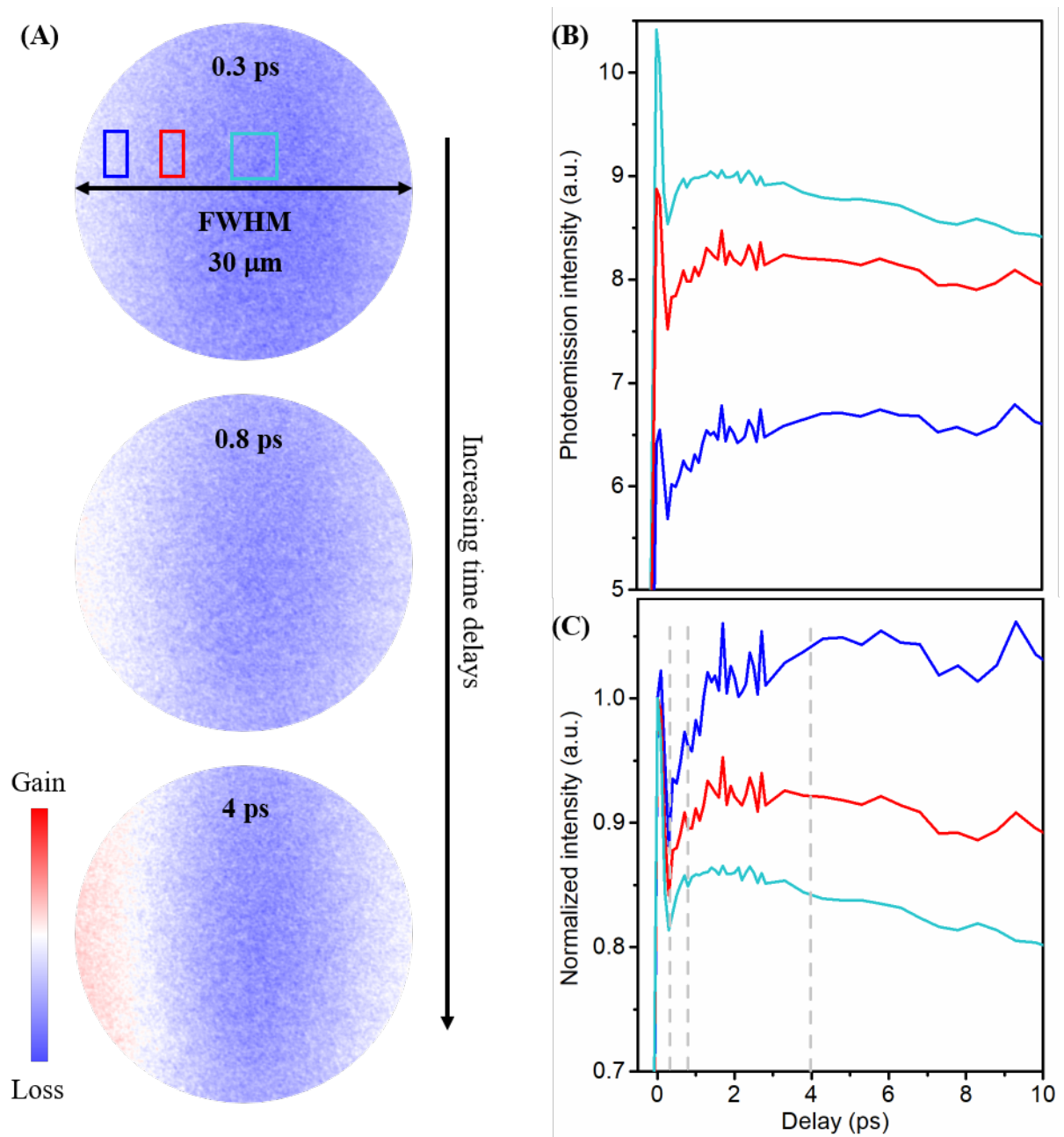
Figure 4.8: Spatial variation in the local carrier dynamics for an intermediate carrier density of 9.3 x 10^{18}cm^{-3}.
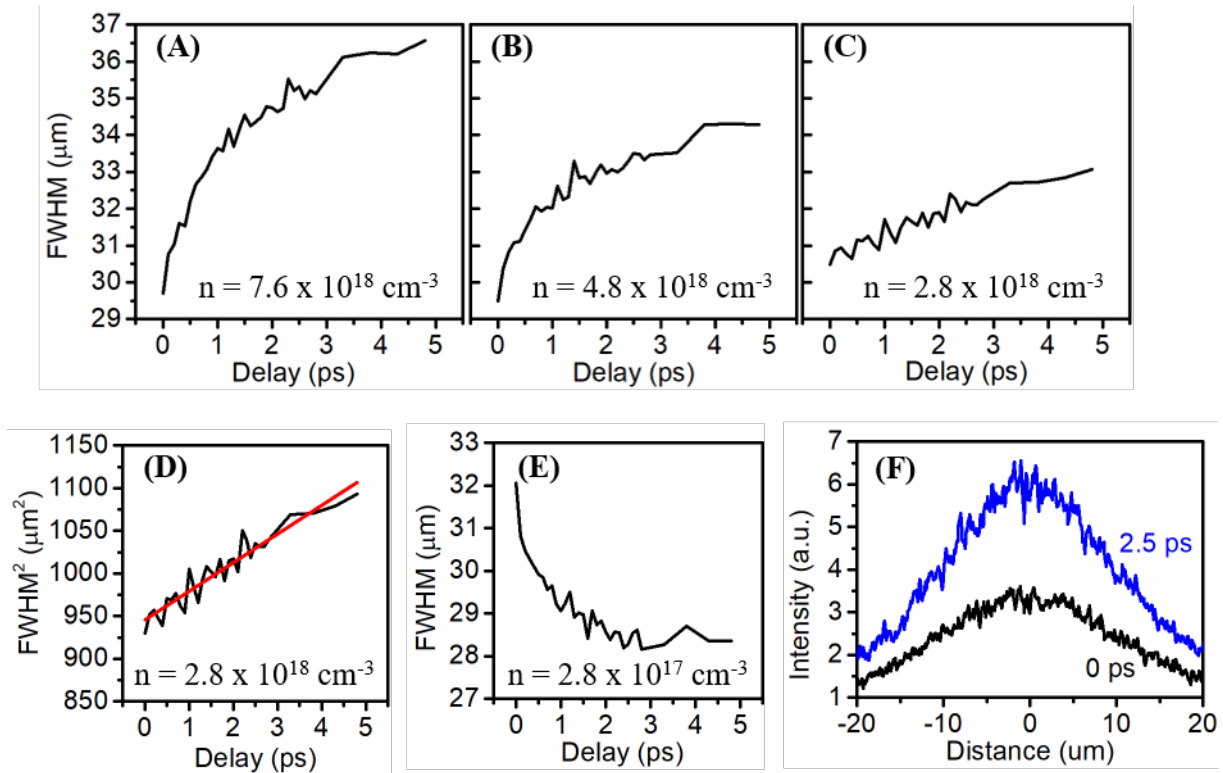
Figure 4.9: From rapid broadening to shrinking of the spatial distribution profile of electrons. (A–C) The Gaussian fit of the time-delayed photoemission intensity profile along the short axis of the pump beam shows a rapid broadening of the electron distribution as more electrons reach the sample surface further away from the center of the beam. (D) As a quantitative comparison for the rate of broadening, the squared width of the time-delayed intensity profile for low carrier density of 2.8 x $10^{18} cm^{-3}$ is plotted. The linear fit shows an equivalent diffusion coefficient of $30{,}000 cm^2/s$. (E) At even lower carrier density of 2.8 x $10^{17} cm^{-3}$, the intensity profile rapidly shrinks by as much as 4μm within the first 2ps. (F) A comparison of the intensity profile at both 0ps and +2.5ps time delays now shows an opposite trend where the gain in the electron density is higher near the center than further away.

photoexcitation (Figure 4.9A). As the carrier density decreases and the vertical transport of electrons start to dominate over the entire photoexcitation spot, the rapid broadening of the intensity profile still persists albeit at a decreasing rate (Figure 4.9B–C). Though the effect of Auger recombination has become negligible at the lower carrier density of 2.8 x $10^{18}cm^{-3}$, the spatially inhomogeneous partial screening of the intrinsic field still leads to a higher gain in the electron density further away from the center than at the center (Figure 4.9C) and as such causes the electron distribution to broaden over time. To provide a quantitative comparison to the rapid rate of broadening, the linear fit of the square width of the time-delayed profile for the low carrier density of 2.8 x $10^{18}cm^{-3}$ shows an equivalent diffusion coefficient of 30,000cm^2/s (Figure 4.9D) which is three orders of magnitude faster than the reported diffusion coefficient of 20cm^2/s in GaAs [47].

In contrast to the rapid broadening, the intensity profile at even lower carrier density of 2.8 x $10^{17}cm^{-3}$ instead shrinks rapidly by as much as 4μm within the first 2ps (Figure 4.9E). An examination of the intensity profile at both 0ps and +2.5ps shows that there is now a higher gain in the electron density near the center of the photoexcitation spot than further away from the center (Figure 4.9F). The decrease in the influx of electrons further away from the center could be due to either a decrease in the drift velocity or a loss of electrons from the Γ-valley (the low probe photon energy limits the momentum space that can be accessed by the instrument as described in Chapter 2). In addition, as the local carrier density decreases further away from the center, the local effective electric field increases due to the lesser degree of screening of the intrinsic field. As such, the lower influx of the photoexcited electrons at higher local effective electric field points towards the onset of intervalley scattering of the electrons from the Γ–valley to the L–valleys. In general, due to the energy difference between the Γ and L minima of 330meV in GaAs [48, 49, 50], the low electron excess energy gained from the 1.55eV pump pulse is not sufficient for intervalley scattering to occur. Instead to gain sufficient energy comparable to the energy difference between the Γ–L valleys, the electrons will have to accelerate efficiently under high field to overcome intravalley scattering and gain sufficient energy

traversing the short length of the depletion region for intervalley scattering to occur [50, 51]. And as the electrons scatter to the L–valleys with higher effective mass, the lower average drift velocity and the reduced number of electrons in the Γ–valley will both contribute to the smaller influx of electrons reaching the sample surface at higher effective electric field.

4.7   Chapter conclusion

In summary, this work shows that the intensity variation that occurs within the photoexcitation beam can be exploited to control the spatiotemporal distribution of the photoexcited charge carriers on the surface of a perfectly homogeneous semiconductor. This finding shows a promising potential for the manipulation of photocarriers beyond the diffraction limit of light. Furthermore, the availability of photocarriers at the surface and the efficient separation of electron-hole pairs are amongst the rate-determining steps in photocatalytic processes. As such, the non-uniform screening of the intrinsic surface field leading to the vertical transport of the photocarriers only at selective spatial regions could lead to the enhancement of spatial selectivity in surface photochemical processes such as photoetching [52, 53] or photodeposition of metal on semiconductor substrates [54]. In addition to the spatial selectivity, the use of an ultrafast light pulse also allows for temporal control of the site-specific surface chemical reactions [55, 56, 57].

Chapter 5

Separation of photoexcited electrons with ultrafast light pulse

5.1 Chapter overview

This chapter studies the manipulation of the lateral distributions of electrons on a homogeneous GaAs sample surface at long time delays. Using TR-PEEM, this chapter first demonstrates the eventual separation of the photoexcited electrons at long time delays for high photoexcited carrier density. It is then further demonstrated that the separation process can be controlled via the spatial profile and intensity of the photoexcitation beam. The chapter then goes on to discuss the spatial variation in the screening of the intrinsic surface field and the buildup of nontrivial lateral electric fields along the sample surface that eventually results in the pulling apart of the electron distributions. A simple model is used to explain the underlying charge transport phenomena and to reproduce the salient features of the experimental data.

5.2   Experimental method

As described in Chapter 3, the in-situ cleaved <110> surface of p-type GaAs is first photoexcited with a 1.55eV pump and then photoemitted with a 4.65eV probe. PEEM then images the spatial distribution of the photoemitted electrons as a function of the pump-probe delays. Both the pump and the probe beams are set to p-polarization and focused onto the sample at a grazing angle of 18°. Due to the grazing angle of incidence, an elliptical photoexcitation beam is formed with a steep Gaussian intensity profile along the short axis and a more gradual profile along the long axis. Further details of the experimental setup can be found in Chapter 3.

5.3   Ultrafast separation of like charges

With the experimental capability, the spatial distributions of the photoexcited electrons are first imaged at several different time delays for both low (1.4 x $10^{18} cm^{-3}$) and high (2.1 x $10^{19} cm^{-3}$) photoexcited carrier densities (Figure 5.1). The normalized photoemission intensities at three different delays are plotted in 3D to highlight the evolution of the electron distribution profiles from the initial photoexcited Gaussian distribution. The white lines in the 2D images projected in the XY-plane mark the FWHM boundaries of the fitted Gaussian distributions.

At the instant of photoexcitation i.e. 0ps, the photoexcited electrons inherit the Gaussian distribution of the pump beam. For low photoexcited carrier density, the spatial distribution of the electrons continues to retain the Gaussian profile as the photocarriers diffuse and recombine over time, as expected for a homogeneous sample (Figure 5.1A). In contrast, at high photoexcited carrier density, the electron spatial distribution at +200ps starts to exhibit significant deviation from a Gaussian distribution. And by +500ps, the photoexcited electrons have split into two distinct distributions with the separation between the two peaks greater than the FWHM of the two separated distributions [58].

The corresponding 2D images showing the evolution of the electron distributions at
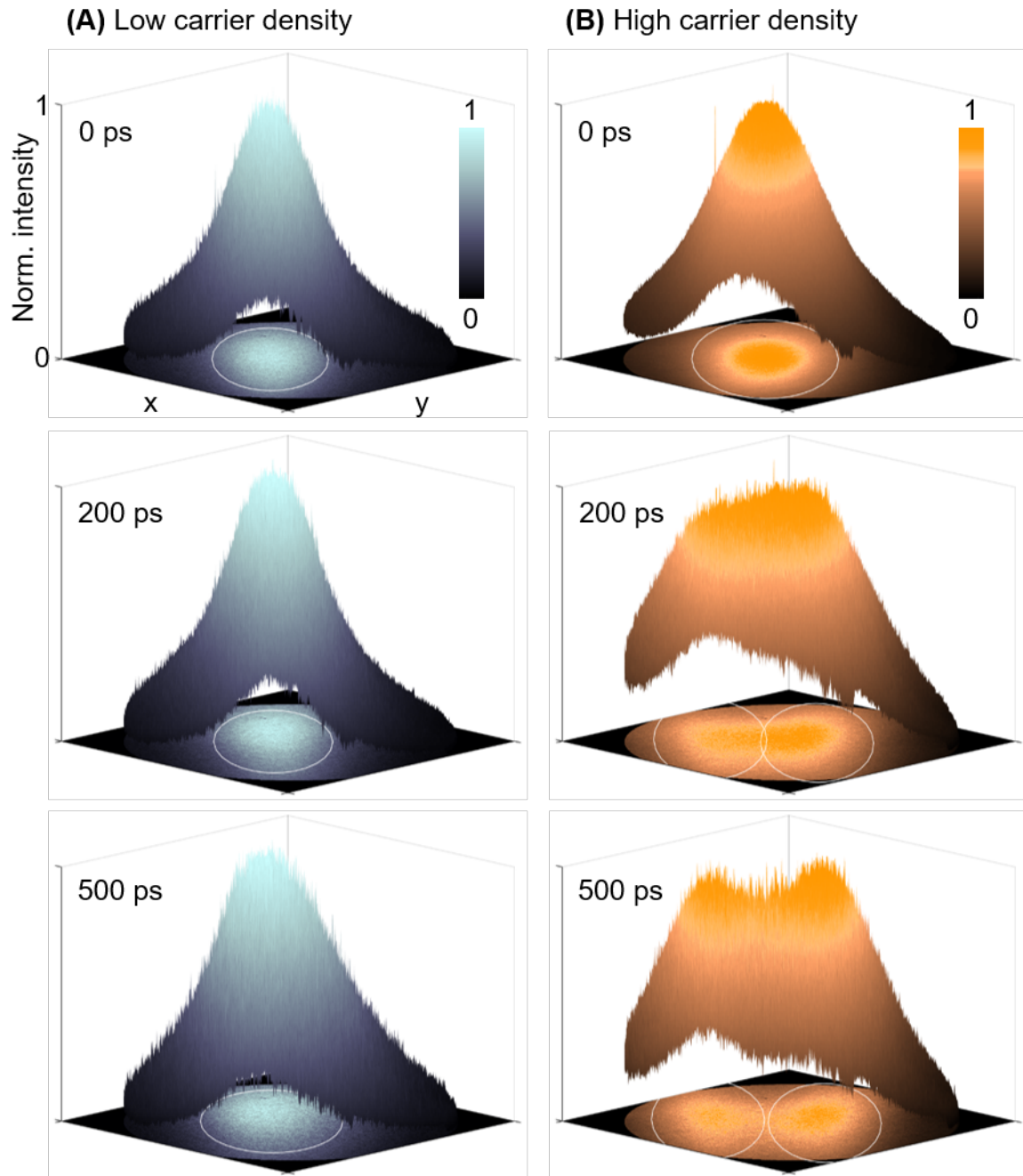
Figure 5.1: Puling apart photoexcited electrons within the pump spot. Normalized spatial distributions of the photoexcited electrons at three different time delays i.e. 0ps, +200ps and +500ps for both (A) low and (B) high photoexcited carrier densities. The white lines in the 2D images mark the FWHM boundaries of the distributions. (A) At low carrier density (1.4 x $10^{18}cm^{-3}$), the photoexcited electrons retain a Gaussian distribution as they undergo diffusion and recombination overtime. (B) At high carrier density (2.1 x $10^{19}cm^{-3}$), the initial Gaussian distribution at 0ps starts to separate at +200ps and eventually split into two distinct distributions at +500ps.
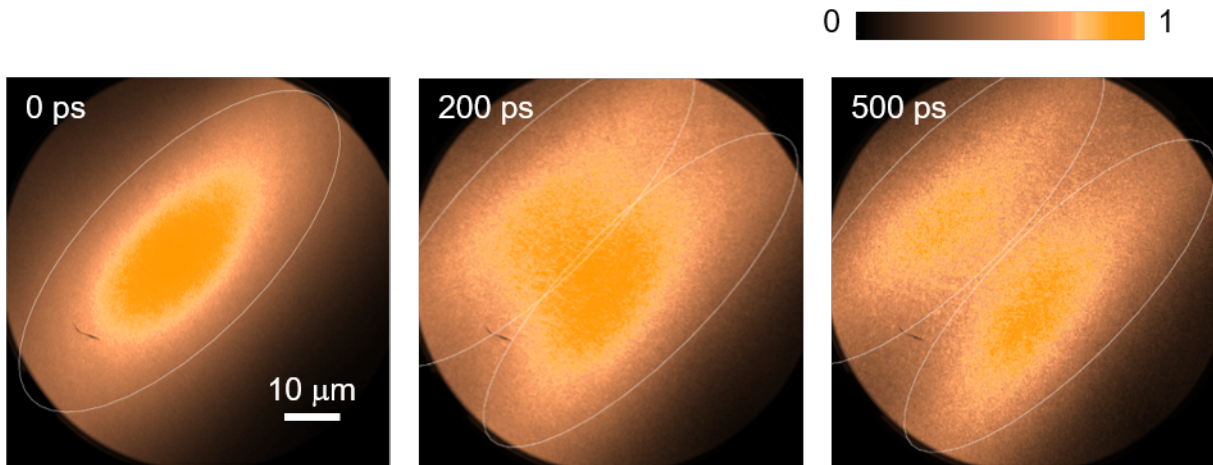
Figure 5.2: 2D images showing the separation of the photoexcited electrons along the short axis of the elliptical pump spot for high carrier density of 2.1 x 10¹⁹cm⁻³. The time-delayed images are normalized individually to highlight the evolution of the electron spatial distributions. The white lines demarcate the FWHM of the fitted Gaussian distributions.

high carrier density are plotted in Figure 5.2. At 0ps, the spatial distribution of the photoexcited electrons exhibits an elliptical profile due to the grazing angle of incidence of the pump beam. Due to the steeper potential gradient, the elliptical profile results in a stronger lateral electric field along the short axis of the photoexcitation spot, as explained in further details later. Due to the anisotropic lateral electric field, the photoexcited electrons start to separate (+200ps) and eventually split into two distinct distributions (+500ps) along the short axis of the elliptical beam spot.

5.4   Controlling the degree and rate of separation

In addition to the spatial profile, the intensity of the photoexcitation beam also provides a control over the degree and rate of separation of the photoexcited electrons. Figure 5.3A shows the electron distribution profile at +500ps for three different photoexcited carrier densities of $2.8 \times 10^{18} cm^{-3}$, $8.4 \times 10^{18} cm^{-3}$ and $2.1 \times 10^{19} cm^{-3}$. At $2.8 \times 10^{18} cm^{-3}$, the electron distribution resembles that of a flat-top Gaussian, hinting at the separation of the photoexcited electrons. At $8.4 \times 10^{18} cm^{-3}$, the electron distribution now clearly shows
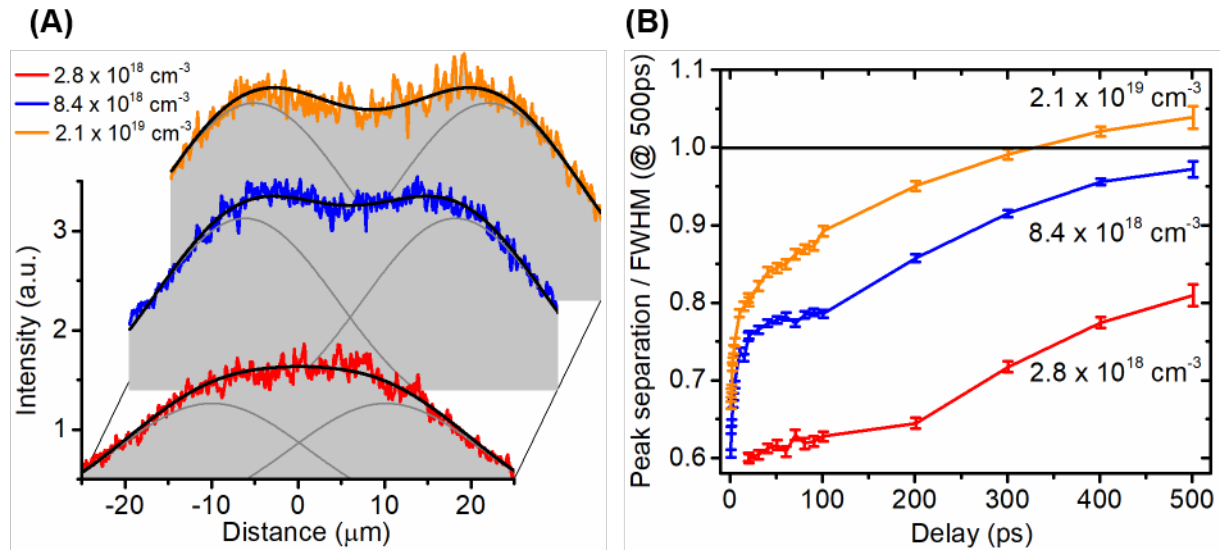
Figure 5.3: Controlling the degree and rate of separation of the photoexcited electrons. (A) The electron distributions at +500ps for three different photoexcited carrier densities. The black line shows the fitted distribution profile that comprises of two overlapping Gaussians with the same width and amplitude (grey lines), leaving only the peak positions as free parameters for fitting. (B) The fitted peak separations are then plotted as a ratio of the FWHM of the distributions at +500ps.

two distinct peaks indicating the presence of two overlapping Gaussian distributions. At $2.1 \times 10^{19} cm^{-3}$, the two distinct peaks have now moved even further apart showing a larger separation between the two overlapping electron distributions.

For quantitative measurement of the separation between the two distinct distributions, the time-delayed distribution profiles are fitted with two Gaussians of the same width and amplitude (grey lines in Figure 5.3A), leaving only the peak positions as free parameters for fitting. The fitted peak separations for the three carrier densities are then plotted as a ratio of the FWHM of their respective distributions at +500ps, as shown in Figure 5.3B. The black line marks the FWHM criterion which states that two overlapping Gaussian distributions are resolvable if the separation between the peaks is equal to the FWHM of the Gaussian distributions [58]. Figure 5.3B clearly shows that the rate and the eventual separation of the photoexcited electrons can be controlled by the photoexcitation intensity.
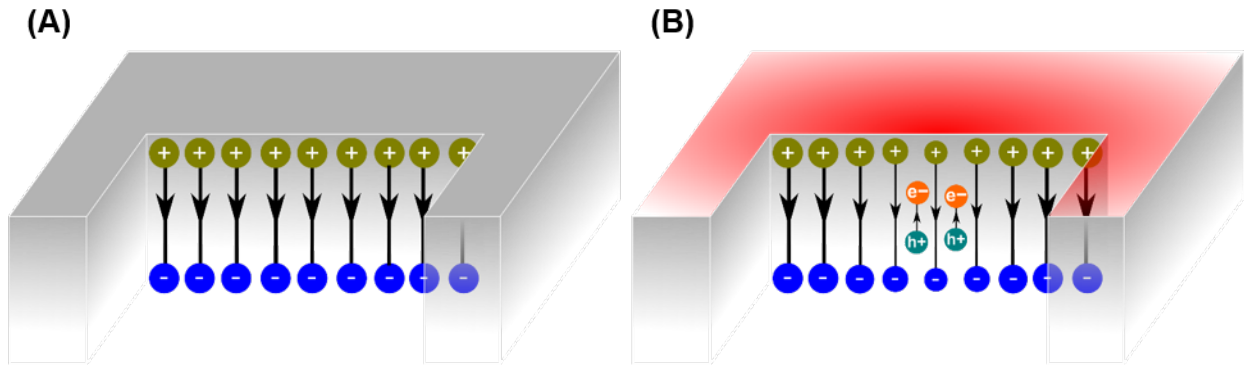
Figure 5.4: Layer of surface dipoles (A) before and (B) after photoexcitation.

5.5 Formation of lateral electric field

To understand the above phenomena, this section first explains the generation of an in-plane electric field due to the intensity variation within the Gaussian pump beam. Prior to photoexcitation, a layer of positively charged surface states exists at the surface of a p-doped semiconductor and is balanced by the negatively charged dopants in the space charge region (SCR) resulting in the well-known band bending in doped semiconductors [32, 46, 59, 60, 61] (Figure 5.4A). Upon photoexcitation, the photocarriers are separated under the influence of the intrinsic field with the photoexcited electrons drifting towards the sample surface and the photoexcited holes towards the bulk. The separation of the photoexcited electron-hole pairs leads to the buildup of an opposite electric field that then partially screens the pre-existing dipoles and diminishes the intrinsic field causing the surface bands to unbend. This phenomena is also known as surface photovoltage effect and has been well-studied in the past as an average effect across the entire optical spot [46, 59, 60].

As demonstrated in the previous chapter, the intensity variation within the photoexcitation beam leads to a spatially inhomogeneous partial screening of the intrinsic field within the pump spot (Figure 5.5). At the center of the spot, the higher density of photocarriers leads to a more effective screening of the intrinsic field resulting in less vertical transport of photocarriers, as evidenced by the smaller increase in the photoemission
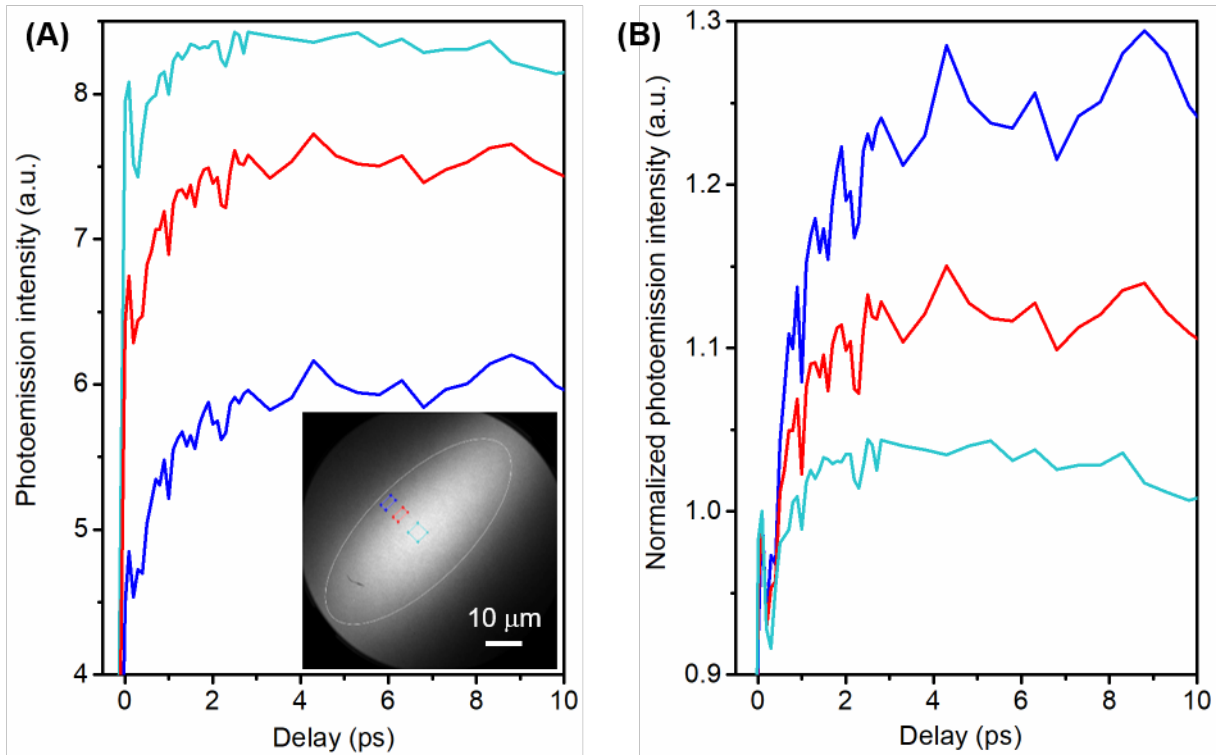
Figure 5.5: Spatially inhomogeneous partial screening of the intrinsic surface field for photoexcited carrier density of 7.0 x 10^{18}cm^{-3}. (A) Time-delayed photoemission intensity measured at three different spatial locations (indicated in the PEEM image in inset). The white line marks the FWHM boundary of the photoexcitation spot (Inset). (B) The three pump-probe curves are normalized at 0ps to highlight the spatially inhomogeneous partial screening of the intrinsic field as shown by the different increase in the photoemission intensity measured at the three different spatial locations.

intensity. Further away from the center, the decreasing carrier density results in diminishing partial screening of the field allowing more photoexcited electrons to drift towards the surface and hence the increasing rise in the photoemission intensity.

The non-uniform screening of the intrinsic surface field results in a laterally varying surface potential (Figure 5.6). At the right intensity, the surface bands at the center of the photoexcitation spot (marked by the origin in Figure 5.6) will be flattened due to the complete screening of the intrinsic field while the bands further away will remain bent due to the partial screening of the field. The difference in the surface potential leads to an in-plane electric field that radiates away from the center of the Gaussian beam.
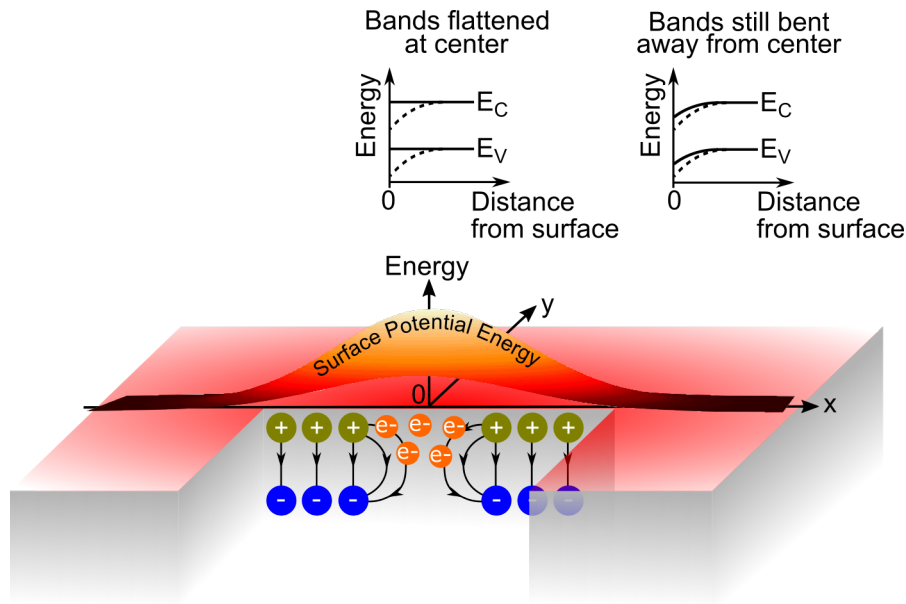
Figure 5.6: Schematic of laterally varying surface potential due to the non-uniform screening of the intrinsic surface field.

The shallower potential gradient along the long axis of the elliptical beam profile weakens the corresponding electric field and thereby ensuring that the photoexcited electrons are pulled apart along the short axis of the elliptical beam (Figure 5.2).

5.6 Dipole model & numerical simulation

To quantitatively modeled the observed phenomena, the intrinsic surface field is modeled as a layer of dipoles separated by the width of the depletion region, w. Due to the non-uniform screening, the dipoles will be fully screened at the center of the photoexcitation spot and partially screened further away resulting in a gradient of unscreened dipoles away from the center (Figure 5.7A-B). The photoexcited electrons at the surface near the center of the pump spot will experience a lateral pull outward, towards the unscreened positive charges on the surface while the unscreened negative charges deeper within will push the electrons back towards the center (Figure 5.7C). Due to the difference in the distance, the photoexcited electrons closer to the positive charges in the $+x$ direction will

experience a net attractive pull towards the +x direction and vice versa for the electrons closer to the positive charges in the -x direction. As such, the electric field due to the positive surface charges at a distance "a" from the center of the pump spot is

$$E_+(a) = -\frac{q}{2\pi\varepsilon_0} \int \sigma[1 - e^{\frac{-x^2}{2c^2}}]\frac{dx}{(x-a)} \tag{5.1}$$

where σ is the surface charge density, q is the electron charge, ε_0 is the vacuum permittivity, and c is the parameter deduced from the width of the Gaussian photoexcitation beam. Correspondingly, the electric field due to the negative charges at z = -w is

$$E_-(a) = \frac{q}{2\pi\varepsilon_0} \int \sigma[1 - e^{\frac{-x^2}{2c^2}}]\frac{(x-a)dx}{(x-a)^2 + w^2} \tag{5.2}$$

Figure 5.7D shows the nontrivial spatially varying resultant electric field that arises due to the non-uniform screening of the layer of dipoles.

With the use of the dipole model to estimate the spatially varying in-plane electric field, the lateral transport of the photoexcited electrons at the sample surface is then modeled with the following drift-diffusion equation:

$$\frac{\delta N(x,t)}{\delta t} = D\nabla^2 N(x,t) + \mu E(x)\nabla N(x,t) - \frac{N(x,t)}{\tau} \tag{5.3}$$

where N is the electron density, D is the diffusion coefficient, μ is the electron mobility, and τ is the recombination rate. As the photoexcited electrons redistribute in the lateral electric field (and recombine), the lateral field will also evolve (and weaken) correspondingly (Figure 5.8A) and in turn impacts the photoexcited electron distribution. As such, the electric field distribution and the electron distribution is calculated iteratively as they evolve in time. By using the three parameters i.e. D, μ and τ as fitting parameters, the separation of the photoexcited electrons can be reproduced qualitatively as shown in Figure 5.8B.
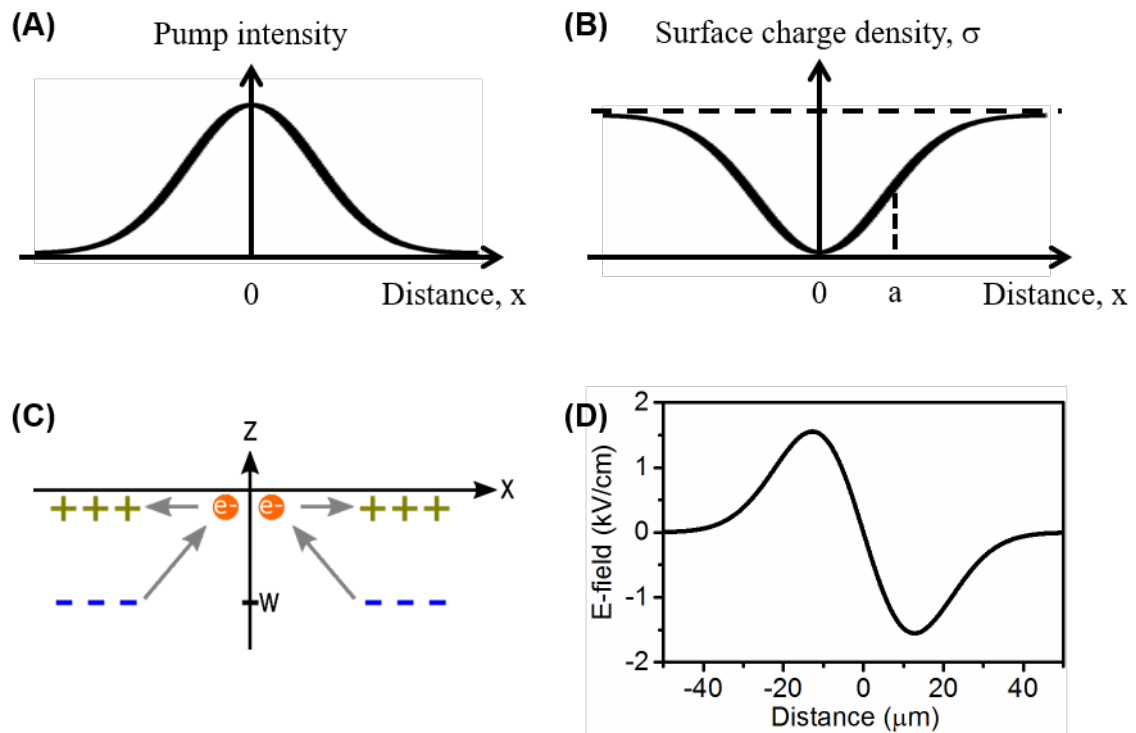
Figure 5.7: Formation of in-plane spatially varying electric field. (A) Schematic illustrating the photoexcitation spot. (B) Gradient of unscreened surface charge density as a function of the distance from the center of the pump beam. (C) Schematic of the dipole model showing unscreened positive charges (dark yellow plus signs) along the surface (z = 0) and unscreened negative charges (blue minus signs) deeper in the bulk (z = -w). The photoexcited electrons (orange balls) at the surface near the center of the pump spot experience a lateral pull outward, towards the positive charges while the negative charges deeper within push the electrons back towards the center of the spot. (D) The nontrivial spatially varying in-plane electric field due to the gradient of unscreened dipoles.
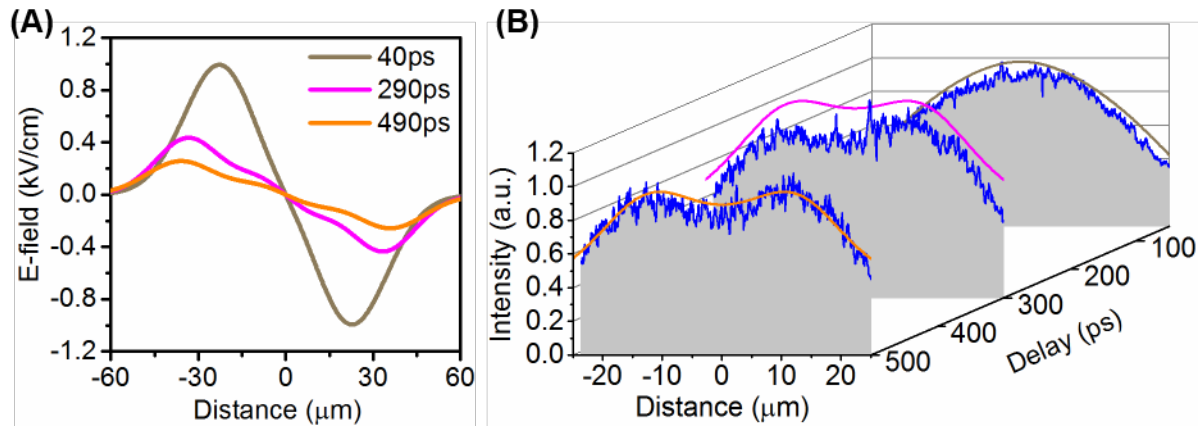
Figure 5.8: Numerical simulation of the evolving lateral electric field and the electron distribution profile for the photoexcited carrier density of 2.1 x 10^{19}cm^{-3}. (A) The spatially varying electric field numerically calculated from the evolving distribution of unscreened surface dipoles. (B) The calculated (solid line) evolution of the photoexcited electron distribution reproduces the salient features of the experimental data (blue lines and grey planes) showing the separation of the photoexcited electrons into two distinct distributions at long time delays. The fitted values of D, μ and τ are $85 cm^2 s^{-1}$, $3300 cm^2 V^{-1} s^{-1}$ and 500ps respectively.

5.7 Chapter conclusion

In summary, this work shows that the spatially inhomogeneous screening of the intrinsic surface field due to the intensity variation within the photoexcitation spot leads to the generation of a nontrivial spatially varying lateral electric field. The formation of the in-plane electric field then acts upon the electrons at the sample surface pulling them apart. Furthermore, depending on the profile and the intensity of the pump beam, the degree and rate of separation of the photoexcited electrons can be controlled.

This work opens up a new avenue in the high resolution spatiotemporal control of the photoexcited charge carriers of the same species. Moreover, the ability to manipulate the photoexcited charge carrier distribution within the pump spot opens up the possibility of control beyond the diffraction limit. With the use of a spatial light modulator, one could arbitrarily imprint a desired intensity pattern on the sample surface and thus achieve arbitrary control of the photoexcited electron distributions on the nanometer and femtosecond

scale. Such control can be used to direct individual branches of charge currents to drive nanoscale optoelectronic devices or to control localized photocatalytic processes. In addition, the use of other semiconducting materials such as transition metal dichalcogenides or topological insulators could lead to more interesting control of the charge currents. For example, the reported higher electron mobility and longer lifetime of multilayer MoS_2 at low temperature [62] are likely to lead to faster initial separation and further peak separation. Another potential study is the electron transport in the topologically protected surface states of Bi_2Se_3 where the transport of the electrons in the linearly dispersive surface states are likely to be different from that in the surface states of traditional bulk semiconductors such as GaAs. Lastly, the ability to create lateral variation in the surface potentials via the control of the surface band bending could also allow for the flow of other quasiparticles such as the neutral, tightly-bound excitons which could potentially lead to next-generation excitonic technologies [63, 64].

Conclusion

Manipulation of the flow and transport of photoexcited charge carriers through materials and across interfaces is ubiquitous in many of modern technologies such as light-harvesting and optoelectronic devices. Achieving control of the spatiotemporal dynamics of the photocarriers using the intensity variation within an ultrafast light pulse could provide a new handle for fast, nanoscale control of the flow and transport of the photocarriers. This thesis presents the work done on manipulating the three-dimensional flow of photoexcited electrons within the optical spot by harnessing the intensity-dependent surface photovoltage (SPV) effect in doped semiconductors. By utilizing the intensity variation within the Gaussian beam, we show that the SPV effect can be exploited for spatially resolved manipulation of the vertical transport of the photocarriers within the beam spot. Furthermore, by leveraging the ability to control the local surface potential energy, we demonstrate that the non-uniform surface potential energy leads to the buildup of a lateral electric field that acts upon the photoexcited electrons on the sample surface pulling them apart.

Experimental setup and sample preparation

For the studies described in this thesis, TR-PEEM is used to allow for the spatiotemporal study of the photocarrier dynamics within the photoexcitation spot. The combination of an ultrafast pump-probe setup together with the PEEM offers the capability to image directly the photoexcited electron distributions on the cleaved <110> surface of the p-doped GaAs sample. As discussed in Chapter 3, the photoemission spectra of the sample show

that despite the large increase in the photoemitted electrons due to the photoexcitation of the sample, the TR-PEEM measurements are not affected by any measurable space charge effect. And by matching the band dispersion in the TR-ARPES measurement of the sample, the two peaks observed in the photoemission spectra are attributed to be the surface states and the conduction band of the GaAs sample. Furthermore, the narrower penetration depth of the 266nm probe pulse compared to the depletion width and the much deeper penetration depth of the 800nm pump pulse has allowed TR-PEEM the capability to resolve the vertical transport of the photocarriers within the space charge region in addition to the lateral transport of photocarriers on the sample surface.

Controlling the vertical transport of photocarriers

For this study, the partial screening of the intrinsic surface field as a function of the photoexcited carrier density is first measured at the center of the photoexcitation spot where the photoexcitation intensity is relatively homogeneous. Then, the photocarrier dynamics at various distances away from the center of the optical spot is measured to demonstrate that the intensity variation within the photoexcitation beam can be used to control the local partial screening of the intrinsic field and thereby achieving spatially resolved control of the vertical transport of the photocarriers. The ability to manipulate the photocarrier dynamics within the optical beam spot allows for the promising potential to control the photocarriers beyond the diffraction limit of light. In addition, the ability to control the separation of the photoexcited electron-hole pairs and the transport of the electrons to the surface at selective spatial regions could enhance the spatial selectivity of photochemical reactions such as photoetching or photodeposition of metals for use in microelectronic fabrications. The spatial selectivity and the use of an ultrafast pulse could also be useful for controlled photocatalytic activities at specific location and time.

Separation of photoexcited electrons with ultrafast light pulse

In this study, the spatially non-uniform partial screening of the intrinsic field as demonstrated in Chapter 4 is leveraged to generate a nontrivial spatially varying lateral electric field. At long delays, the presence of the lateral electric field eventually separates the photoexcited electrons into two distinct distributions. It is further demonstrated that the degree and rate of separation of the electron distribution can be controlled via the profile and intensity of the pump beam. The ability to manipulate and separate charge carriers of the same species within the optical spot at ultrafast time scale could lead to a new avenue in optoelectronic control. In addition, the induced lateral electric field presented in this work could be used to study the transport of surface electrons in other semiconducting materials such as transition metal dichalcogenides or topological insulators which could provide more interesting control of the charge currents. Furthermore, the manipulation of the lateral surface potential energy could potentially be applied for controlling the flow of other quasi-particles such as excitons which could potentially lead to future excitonic devices.

Bibliography

[1] Zhi Guo, Yan Wan, Mengjin Yang, Jordan Snaider, Kai Zhu, and Libai Huang. Long-range hot-carrier transport in hybrid perovskites visualized by ultrafast microscopy. *Science*, 356(6333):59–62, 2017. 3, 6

[2] Hui Ling Tan, Rose Amal, and Yun Hau Ng. Alternative strategies in improving the photocatalytic and photoelectrochemical activities of visible light-driven BiVO_4: a review. *J. Mater. Chem. A*, 5(32):16498–16521, 2017. 4

[3] Brian P. Mehl, Justin R. Kirschbrown, Michelle M. Gabriel, Ralph L. House, and John M. Papanikolas. Pump-probe microscopy: Spatially resolved carrier dynamics in ZnO rods and the influence of optical cavity resonator modes. *Journal of Physical Chemistry B*, 117(16):4390–4398, 2013. 6

[4] S. Nah, B. Spokoyny, C. Stoumpos, C. M.M. Soe, M. Kanatzidis, and E. Harel. Spatially segregated free-carrier and exciton populations in individual lead halide perovskite grains. *Nature Photonics*, 11:285–288, 2017. 6

[5] M. A. Seo, J. Yoo, S. A. Dayeh, S. T. Picraux, A. J. Taylor, and R. P. Prasankumar. Mapping carrier diffusion in single silicon core-shell nanowires with ultrafast optical microscopy. *Nano Letters*, 12(12):6334–6338, 2012. 6

[6] Michelle M. Gabriel, Justin R. Kirschbrown, Joseph D. Christesen, Christopher W. Pinion, David F. Zigler, Erik M. Grumstrup, Brian P. Mehl, Emma E M Cating, James F. Cahoon, and John M. Papanikolas. Direct imaging of free carrier and trap

carrier motion in silicon nanowires by spatially-separated femtosecond pump-probe microscopy. *Nano Letters*, 13(3):1336–1340, 2013. 6

[7] Michelle M. Gabriel, Erik M. Grumstrup, Justin R. Kirschbrown, Christopher W. Pinion, Joseph D. Christesen, David F. Zigler, Emma E M Cating, James F. Cahoon, and John M. Papanikolas. Imaging charge separation and carrier recombination in nanowire p-i-n junctions using ultrafast microscopy. *Nano Letters*, 14(6):3079–3087, 2014. 6

[8] Zhi Guo, Joseph S. Manser, Yan Wan, Prashant V. Kamat, and Libai Huang. Spatial and temporal imaging of long-range charge transport in perovskite thin films by ultrafast microscopy. *Nature Communications*, 6:7471, 2015. 6

[9] Bolin Liao and Ebrahim Najafi. Scanning ultrafast electron microscopy: A novel technique to probe photocarrier dynamics with high spatial and temporal resolutions. *Materials Today Physics*, 2:46–53, 2017. 6

[10] Ebrahim Najafi, Timothy D Scarborough, Jau Tang, and Ahmed Zewail. Four-dimensional imaging of carrier interface dynamics in p-n junctions. *Science*, 347(6218):164–167, 2015. 6

[11] Bolin Liao, Ebrahim Najafi, Heng Li, Austin J. Minnich, and Ahmed H. Zewail. Photo-excited hot carrier dynamics in hydrogenated amorphous silicon imaged by 4D electron microscopy. *Nature Nanotechnology*, 12:871–876, 2017. 6

[12] Bolin Liao, Huan Zhao, Ebrahim Najafi, Xiaodong Yan, He Tian, Jesse Tice, Austin J. Minnich, Han Wang, and Ahmed H. Zewail. Spatial-temporal imaging of anisotropic photocarrier dynamics in black phosphorus. *Nano Letters*, 17(6):3675–3680, 2017. 6

[13] E. Bauer. Cathode lens electron microscopy: Past and future. *Journal of Physics: Condensed Matter*, 21(31):314001, 2009. 8, 9, 11

[14] Ernst Bauer. A brief history of PEEM. *Journal of Electron Spectroscopy and Related Phenomena*, 185(10):314–322, 2012. 8, 12

[15] Ernst Bauer. LEEM and UHV-PEEM: A retrospective. *Ultramicroscopy*, 119:18–23, 2012. 8

[16] Elmitec. PEEM III. https://elmitec.de/Peem.php?Bereich=PEEM3, [Online; accessed on 15 May 2018]. 8

[17] E. Bauer. Photoelectron microscopy. *Journal of Physics: Condensed Matter*, 13(49):11391–11404, 2001. 10

[18] Elmitec. Hemispherical imaging energy analyzer. https://elmitec.de/Components.php?Bereich=Analyzer, [Online; accessed 15-May-2018]. 11

[19] Zhirong Huang. Brightness and coherence of synchrotron radiation and FELs. In Zhimin Dai, Christine Petit-Jean-Genaz, Volker R. W. Schaa, and Chuan Zhang, editors, *Proceedings of IPAC2013*, pages 16–20, Shanghai, 2013. 12

[20] Steffen Hädrich, Arno Klenke, Jan Rothhardt, Manuel Krebs, Armin Hoffmann, Oleg Pronin, Vladimir Pervak, Jens Limpert, and Andreas Tünnermann. High photon flux table-top coherent extreme-ultraviolet source. *Nature Photonics*, 8:779–783, 2014. 15

[21] I. Pupeza, S. Holzberger, T. Eidam, H. Carstens, D. Esser, J. Weitenberg, P. Rußbüldt, J. Rauschenberger, J. Limpert, Th Udem, A. Tünnermann, T. W. Hänsch, A. Apolonski, F. Krausz, and E. Fill. Compact high-repetition-rate source of coherent 100 eV radiation. *Nature Photonics*, 7:608–612, 2013. 15

[22] Atsushi Kubo, Ken Onda, Hrvoje Petek, Zhijun Sun, Yun S Jung, and Hong Koo Kim. Femtosecond imaging of surface plasmon dynamics in a nanostructured silver film. *Nano Letters*, 5(6):1123–1127, 2005. 15, 16

[23] Christoph Lemke, Till Leißner, Andrey Evlyukhin, Jörn W. Radke, Alwin Klick, Jacek Fiutowski, Jakob Kjelstrup-Hansen, Horst Günter Rubahn, Boris N. Chichkov, Carsten Reinhardt, and Michael Bauer. The interplay between localized and propagating plasmonic excitations tracked in space and time. *Nano Letters*, 14(5):2431–2435, 2014. 16

[24] Philip Kahl, Daniel Podbiel, Christian Schneider, Andreas Makris, Simon Sindermann, Christian Witt, Deirdre Kilbane, Michael Horn von Hoegen, Martin Aeschlimann, and Frank Meyer zu Heringdorf. Direct observation of surface plasmon polariton propagation and interference by time-resolved imaging in normal-incidence two photon photoemission microscopy. *Plasmonics*, 13(1):239–246, 2018. 16

[25] Shijing Tan, Adam Argondizzo, Jindong Ren, Liming Liu, Jin Zhao, and Hrvoje Petek. Plasmonic coupling at a metal/semiconductor interface. *Nature Photonics*, 11:806–812, 2017. 16

[26] Keiki Fukumoto, Yuki Yamada, Ken Onda, and Shin-Ya Koshihara. Direct imaging of electron recombination and transport on a semiconductor surface by femtosecond time-resolved photoemission electron microscopy. *Applied Physics Letters*, 104(5):053117, 2014. 16, 17

[27] Keiki Fukumoto, Ken Onda, Yuki Yamada, Takashi Matsuki, Tatsuhiko Mukuta, Sei-ichi Tanaka, and Shin-ya Koshihara. Femtosecond time-resolved photoemission electron microscopy for spatiotemporal imaging of photogenerated carrier dynamics in semiconductors. *Review of Scientific Instruments*, 85(8):083705, 2014. 16, 17

[28] Michael K.L. Man, Athanasios Margiolakis, Skylar Deckoff-Jones, Takaaki Harada, E Laine Wong, M. Bala Murali Krishna, Julien Madéo, Andrew Winchester, Sidong Lei, Robert Vajtai, Pulickel M. Ajayan, and Keshav M. Dani. Imaging the motion of electrons across semiconductor heterojunctions. *Nature Nanotechnology*, 12:36–40, 2017. 16, 17, 19

[29] Keiki Fukumoto, Mohamed Boutchich, Hakim Arezki, Ken Sakurai, Daniela Di Felice, Yannick J. Dappe, Ken Onda, and Shin ya Koshihara. Ultrafast electron dynamics in twisted graphene by femtosecond photoemission electron microscopy. *Carbon*, 124:49–56, 2017. 16, 17

[30] F Rotermund and V Petrov. Generation of the fourth harmonic of a femtosecond Ti:sapphire laser. *Optics Letters*, 23(13):1040–1042, 1998. 19

[31] Elmitec. SPELEEM. https://elmitec.de/Leem.php?Bereich=SPELEEM, [Online, accessed on 16-May-2018]. 21

[32] Z. W. Deng, R. W.M. Kwok, W. M. Lau, and L. L. Cao. Time-resolved measurement of surface band bending of cleaved GaAs(110) and InP(110) by high resolution XPS. *Applied Surface Science*, 158(1-2):58–63, 2000. 23, 54

[33] D. E. Eastman and J. L. Freeouf. Photoemission partial yield measurements of unoccupied intrinsic surface states for Ge(111) and GaAs(110). *Physical Review Letters*, 33(27):1601–1605, 1974. 23

[34] W. E. Spicer, I. Lindau, P. E. Gregory, C. M. Garner, P. Pianetta, and P. W. Chye. Synchrotron radiation studies of electronic structure and surface chemistry of GaAs, GaSb, and InP. *Journal of Vacuum Science and Technology*, 13(4):780–785, 1976. 23

[35] W. E. Spicer, P. W. Chye, P. R. Skeath, C. Y. Su, and I. Lindau. New and unified model for Schottky barrier and III–V insulator interface states formation. *Journal of Vacuum Science and Technology*, 16(5):1422–1433, 1979. 23

[36] D. E. Eastman, T. C. Chiang, P. Heimann, and F. J. Himpsel. Surface core-level binding-energy shifts for GaAs(110) and GaSb(110). *Physical Review Letters*, 45(8):656–659, 1980. 23

[37] N. Newman, W. E. Spicer, T. Kendelewicz, and I. Lindau. On the Fermi level pinning behavior of metal/III–V semiconductor interfaces. *Journal of Vacuum Science and Technology*, 4(4):931–938, 1986. 23

[38] U. Semmler, M. Simon, Ph Ebert, and K. Urban. Stoichiometry changes by selective vacancy formation on (110) surfaces of III-V semiconductors: Influence of electronic effects. *Journal of Chemical Physics*, 114(1):445–451, 2001. 23

[39] W. E. Spicer, Z. Liliental-Weber, E. Weber, N. Newman, T. Kendelewicz, R. Cao, C. McCants, P. Mahowald, K. Miyano, and I. Lindau. The advanced unified defect model for Schottky barrier formation. *Journal of Vacuum Science & Technology B: Microelectronics and Nanometer Structures*, 6(4):1245–1251, 1988. 23

[40] Eugene J. Mele and J. D. Joannopoulos. Double-dangling-bond defects and band bending at the GaAs (110) surface. *Physical Review B*, 19(6):2928–2932, 1979. 23

[41] W. E. Spicer, P. W. Chye, C. M. Garner, I. Lindau, and P. Pianetta. The surface electronic structure of 3-5 compounds and the mechanism of Fermi level pinning by oxygen (passivation) and metals (Schottky barriers). *Surface Science*, 86:763–788, 1979. 23

[42] Simon M. Sze and Kwok K. Ng. *Physics of Semiconductor Devices*. John Wiley & Sons, Inc., 3rd edition, 2007. 24

[43] D. E. Aspnes and A. A. Studna. Dielectric functions and optical parameters of Si, Ge, GaP, GaAs, GaSb, InP, InAs, and InSb from 1.5 to 6.0 eV. *Physical Review B*, 27(2):985–1009, 1983. 24

[44] G. E. Jellison. Optical functions of GaAs, GaP, and Ge determined by two-channel polarization modulation ellipsometry. *Optical Materials*, 1(3):151–160, 1992. 24

[45] J. F. James. *A student's guide to Fourier transforms: With applications in physics and engineering*. Cambridge University Press, 3rd edition, 2011. 28

[46] T. Dekorsy, T. Pfeifer, W. Kütt, and H. Kurz. Subpicosecond carrier transport in GaAs surface-space-charge fields. *Physical Review B*, 47(7):3842–3849, 1993. 37, 54

[47] Brian A. Ruzicka, Lalani K. Werake, Hassana Samassekou, and Hui Zhao. Ambipolar diffusion of photoexcited carriers in bulk GaAs. *Applied Physics Letters*, 97(26):262119, 2010. 47

[48] M. Cheng and E. E. Kunhardt. Electron energy distributions, transport parameters, and rate coefficients in GaAs. *Journal of Applied Physics*, 63(7):2322–2330, 1988. 47

[49] J Požela and A Reklaitis. Electron transport properties in GaAs at high electric fields. *Solid-State Electronics*, 23(9):927–933, 1980. 47

[50] A. Leitenstorfer, S. Hunsche, J. Shah, M. C. Nuss, and W. H. Knox. Femtosecond charge transport in polar semiconductors. *Physical Review Letters*, 82(25):5140–5143, 1999. 47, 48

[51] A Leitenstorfer, S Hunsche, J Shah, M C Nuss, and W H Knox. Femtosecond high-field transport in compound semiconductors. *Physical Review B*, 61(24):16642–16652, 2000. 48

[52] Junhui Lai, Ding Yuan, Pei Huang, Jie Zhang, Jian Jia Su, Zhao Wu Tian, and Dongping Zhan. Kinetic investigation on the photoetching reaction of n-type GaAs by scanning electrochemical microscopy. *Journal of Physical Chemistry C*, 120(30):16446–16452, 2016. 48

[53] Adele C. Tamboli, Asako Hirai, Shuji Nakamura, Steven P. DenBaars, and Evelyn L. Hu. Photoelectrochemical etching of p-type GaN heterostructures. *Applied Physics Letters*, 94:151113, 2009. 48

[54] C. Scheck, Y. K. Liu, P. Evans, R. Schad, A. Bowers, G. Zangari, J. R. Williams, and T. F. Issacs-Smith. Photoinduced electrochemical deposition of Cu on p-type Si sub-

strates. *Physical Review B - Condensed Matter and Materials Physics*, 69(3):035334, 2004. 48

[55] Chuanyao Zhou, Zefeng Ren, Shijing Tan, Zhibo Ma, Xinchun Mao, Dongxu Dai, Hongjun Fan, Xueming Yang, Jerry LaRue, Russell Cooper, Alec M. Wodtke, Zhuo Wang, Zhenyu Li, Bing Wang, Jinlong Yang, and Jianguo Hou. Site-specific photocatalytic splitting of methanol on $TiO_2(110)$. *Chemical Science*, 1(5):575–580, 2010. 48

[56] Xuemei Zhou, Ning Liu, and Patrik Schmuki. Photocatalysis with TiO_2 nanotubes: "Colorful" reactivity and designing site-specific photocatalytic centers into TiO_2 nanotubes. *ACS Catalysis*, 7(5):3210–3235, 2017. 48

[57] Shunichi Fukuzumi and Kei Ohkubo. Selective photocatalytic reactions with organic photocatalysts. *Chemical Science*, 4(2):561–574, 2013. 48

[58] J. Gordon Robertson. Quantifying resolving power in astronomical spectra. *Publications of the Astronomical Society of Australia*, 30:e048, 2013. 50, 53

[59] P. Siffalovic, M. Drescher, and U. Heinzmann. Femtosecond time-resolved core-level photoelectron spectroscopy tracking surface photovoltage transients on p-GaAs. *Europhysics Letters*, 60(6):924–930, 2002. 54

[60] W Widdra, D Bröcker, T Gießel, I.V Hertel, W Krüger, A Liero, F Noack, V Petrov, D Pop, P.M Schmidt, R Weber, I Will, and B Winter. Time-resolved core level photoemission: surface photovoltage dynamics of the $SiO_2/Si(100)$ interface. *Surface Science*, 543(1-3):87–94, 2003. 54

[61] Leeor Kronik and Yoram Shapira. Surface photovoltage phenomena: theory, experiment, and applications. *Surface Science Reports*, 37(1-5):1–206, 1999. 54

[62] Jared H. Strait, Parinita Nene, and Farhan Rana. High intrinsic mobility and ultra-fast carrier dynamics in multilayer metal-dichalcogenide MoS_2. *Physical Review B*, 90(24):245402, 2014. 60

[63] Gleb M. Akselrod, Parag B. Deotare, Nicholas J. Thompson, Jiye Lee, William A. Tisdale, Marc A. Baldo, Vinod M. Menon, and Vladimir Bulovic. Visualization of exciton transport in ordered and disordered molecular solids. *Nature Communications*, 5:3646, 2014. 60

[64] Jun Xiao, Mervin Zhao, Yuan Wang, and Xiang Zhang. Excitons in atomically thin 2D semiconductors and their applications. *Nanophotonics*, 6(6):1309–1328, 2017. 60